Pseudospin resonances reveal synthetic spin-orbit interaction

Christoph Rohrmeier* and Andrea Donarini
Institute of Theoretical Physics, University of Regensburg, 93053 Regensburg, Germany

(Received 25 August 2020; revised 3 March 2021; accepted 27 April 2021; published 17 May 2021)

We investigate a spinful double quantum dot coupled to leads in a pseudospin valve configuration. The interplay of interaction and interference produces, in the stability diagram, a rich variety of current resonances modulated by the system parameters. In the presence of ferromagnetic leads and pseudospin anisotropy, those resonances split, turn into dips, and acquire a Fano shape, thus revealing a synthetic spin-orbit interaction induced on the double quantum dot. A set of rate equations derived for a minimal model captures those features. The model accurately matches the numerical results obtained for the full system in the framework of a generalized master equation and calculated within the next to leading order approximation.

DOI: 10.1103/PhysRevB.103.205420

I. INTRODUCTION

Quantum dots (QDs) are characterized by a charging energy and by a discrete energy spectrum, both originating from the spatial confinement of their electronic wave functions. The many-body spectrum of QDs is probed in great detail by coupling them weakly to metallic leads and measuring their transport characteristics as a function of bias and gate voltage. The sequential tunneling of electrons, hopping from source to drain through the dots, typically produces a differential conductance with Coulomb diamonds decorated by parallel resonant lines which are the spectroscopic signatures of the charging energy and the discrete many-body spectrum.

Degeneracies [1] enrich the sequential tunneling dynamics with interference effects. The latter originate from the coherent superposition of the degenerate states which arise in this *coherent-sequential-tunneling* (CST) regime and are modulated by the external parameters like the bias and gate voltage. For a spinful level coupled to noncollinearly polarized ferromagnetic leads (a QD spin valve), interference between the degenerate spin states induces spin accumulation, precession, and relaxation, with a resulting nonequilibrium spin polarization of the dot [2–9] and spin torque on the leads [10].

For a QD spin valve with almost antiparallel lead polarization, a novel spin resonance has been predicted in [11] within the one-particle Coulomb diamond. A crucial role in this phenomenon is played by the exchange magnetic field [2] generated by virtual electronic fluctuations between the dot and the leads, i.e., the Lamb shift correction to the dot Hamiltonian. Orbitally degenerate states support as well interference if combined with couplings to the leads which mix the tunneling channels [12,13], as has been demonstrated for semiconductor wires [14,15], QD molecules [16–22], single-molecule junctions [20,23,24], and suspended carbon nanotubes (CNTs) [25]. Moreover, exchange magnetic fields are able to alter the symmetry of Kondo states [26].

The control of a QD spin valve is a paradigmatic example of *spintronics*. *Valleytronics* concerns instead the manipulation of a state living in a twofold orbitally degenerate space. Very recently, this concept has been further extended to *flavortronics* [27], for interacting systems with n-fold degeneracy.

In this article, we investigate the interplay between valleytronics and spintronics, between the pseudospin of a double quantum dot (DQD) with orbital degeneracy and the spin polarization of the ferromagnetic leads. The spatial decay of the Coulomb interaction implies a pseudospin anisotropy on the DQD. In the presence of ferromagnetic leads, synthetic spin-orbit interaction (SOI) emerges. The synthetic SOI intertwines the spin and the pseudospin degrees of freedom and is revealed by a set of current resonances which split, turn into dips, and acquire a Fano shape by changing the spin polarization of the leads.

The paper is organized as follows: In Sec. II the model for the DQD single-electron transistor in Fig. 1 is introduced, with particular emphasis on the form of the tunneling rate matrices characterizing the coupling between the leads and the system. Section III is dedicated to the quantum transport theory in the Liouville approach which underlies the calculation of the transport characteristics for the system. The numerical results and their interpretation in terms of a minimal model are discussed in Sec. IV. A brief summary and concluding remarks are given in Sec. V.

II. MODEL

The spinful DQD coupled to ferromagnetic leads, schematically shown in Fig. 1, is described by the system-bath Hamiltonian

$$\hat{H} = \hat{H}_{\mathrm{DQD}} + \hat{H}_{\mathrm{leads}} + \hat{H}_{\mathrm{tun}} \tag{1}$$

in which we distinguish, respectively, the DQD, the leads, and the tunneling component. The DQD Hamiltonian is the one of

*christoph.rohrmeier@ur.de

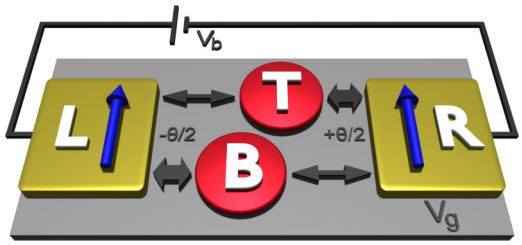

FIG. 1. Schematic setup of a DQD in a pseudospin valve configuration: The left lead (L) is more strongly coupled to the bottom dot (B), the right lead (R) to the top dot (T). The opening angle $\theta \lesssim \pi$ between the pseudospin polarization of the leads ensures the mixing of the pseudospin states during the tunneling event. The bias voltage (V_b) applied to the leads and the gate voltage (V_g) control together the transport characteristics of the DQD. The blue arrows indicate the parallel spin polarization of the leads.

a spinful interacting double-level system

$$\hat{H}_\mathrm{DQD} = \sum_{i=\mathrm{T,B}} [(eV_\mathrm{g} + \varepsilon_0)\hat{n}_i + U\hat{n}_{i\uparrow}\hat{n}_{i\downarrow}] + V\hat{n}_\mathrm{T}\hat{n}_\mathrm{B}, \quad (2)$$

where $\hat{n}_{i\sigma} = \hat{d}^\dagger_{i\sigma}\hat{d}_{i\sigma}$ counts the number of electrons on the ith dot with spin σ, being $\hat{d}_{i\sigma}$ the corresponding electronic annihilation operator, e the electronic charge, and $\hat{n}_i = \sum_\sigma \hat{n}_{i\sigma}$. Moreover, $\hat{H}_\mathrm{DQD}$ contains the on-site energy ε_0 shifted by a gate voltage V_g, as well as U and V, respectively the local and the interdot Coulomb interaction. In general, we expect $U > V$ as it is energetically more favorable to distribute electrons on two separated dots, rather than to confine them on the same one, due to the decay of the Coulomb interaction as a function of the distance between the involved electrons.

For the understanding of the interference effects presented later, it is convenient to express $\hat{H}_\mathrm{DQD}$ in terms of a pseudospin associated with the orbital degree of freedom ($i = \mathrm{T, B}$). We introduce to this end the three components of the pseudospin operator

$$\hat{T}_\alpha = \frac{1}{2}\sum_{\tau ij} \hat{d}^\dagger_{i\tau}\sigma^\alpha_{ij}\hat{d}_{j\tau}, \quad (3)$$

where $\alpha = x, y, z$ and σ^α are the Pauli matrices. The (total) pseudospin operator is given by $\hat{T}^2 = \hat{T}_x^2 + \hat{T}_y^2 + \hat{T}_z^2$. We further notice that the occupation numbers for the top and bottom dot can be expressed as

$$\hat{n}_\mathrm{T,B} = \frac{\hat{N}}{2} \pm \hat{T}_z, \quad (4)$$

where $\hat{N} = \hat{n}_\mathrm{T} + \hat{n}_\mathrm{B}$ is the total particle number operator of the system. Hence, we can reformulate the Hamiltonian as

$$\hat{H}_\mathrm{DQD} = \left(\varepsilon - \frac{U}{2}\right)\hat{N} + \frac{U+V}{4}\hat{N}^2 + (U-V)\hat{T}_z^2, \quad (5)$$

where $\varepsilon = eV_\mathrm{g} + \varepsilon_0$. In this representation, the difference between the local and intersite Coulomb repulsion appears as an easy-plane anisotropy of the pseudospin as seen in the last term of Eq. (5). The latter vanishes in the zero- and four-particle subspaces (both pseudospin singlets) while it reduces to a constant energy shift when evaluated on the one- and the three-particle subspaces (corresponding both to pseudospin doublets).

Most importantly, we can classify the vectors of the two-particle subspace according to their spin and pseudospin. The spin-singlet, pseudospin-triplet states

$$\begin{aligned} |S=0, T_z=+1\rangle &= \hat{d}^\dagger_{\mathrm{T}\uparrow}\hat{d}^\dagger_{\mathrm{T}\downarrow}|\emptyset\rangle, \\ |S=0, T_z=\ \ 0\rangle &= \frac{1}{\sqrt{2}}(\hat{d}^\dagger_{\mathrm{T}\uparrow}\hat{d}^\dagger_{\mathrm{B}\downarrow} - \hat{d}^\dagger_{\mathrm{T}\downarrow}\hat{d}^\dagger_{\mathrm{B}\uparrow})|\emptyset\rangle, \\ |S=0, T_z=-1\rangle &= \hat{d}^\dagger_{\mathrm{B}\uparrow}\hat{d}^\dagger_{\mathrm{B}\downarrow}|\emptyset\rangle \end{aligned} \quad (6)$$

are complemented by the spin-triplet, pseudospin-singlet ones

$$\begin{aligned} |S_z=+1, T=0\rangle &= \hat{d}^\dagger_{\mathrm{T}\uparrow}\hat{d}^\dagger_{\mathrm{B}\uparrow}|\emptyset\rangle, \\ |S_z=\ \ 0, T=0\rangle &= \frac{1}{\sqrt{2}}(\hat{d}^\dagger_{\mathrm{T}\uparrow}\hat{d}^\dagger_{\mathrm{B}\downarrow} + \hat{d}^\dagger_{\mathrm{T}\downarrow}\hat{d}^\dagger_{\mathrm{B}\uparrow})|\emptyset\rangle, \\ |S_z=-1, T=0\rangle &= \hat{d}^\dagger_{\mathrm{T}\downarrow}\hat{d}^\dagger_{\mathrm{B}\downarrow}|\emptyset\rangle. \end{aligned} \quad (7)$$

It is only on the pseudospin-triplet component of the two-particle subspace, spanned by the vectors in Eq. (6), that one appreciates the anisotropy: It is energetically more favorable for the pseudospin vector to be in the x-y plane rather than to point toward the z direction as it costs additional energy to localize both electrons on the same dot.

The DQD is tunnel-coupled to the leads, fermionic baths described by the Hamiltonian $\hat{H}_\mathrm{leads} = \sum_b \varepsilon_b \hat{c}^\dagger_b \hat{c}_b$, where the collective lead index $b = \{l\boldsymbol{k}\sigma_l\}$ comprises $l = \mathrm{L, R}$ labeling the left or right lead, $\boldsymbol{k}$ the momentum vector, indicated in boldface, as all other vectors in this work, and σ_l the spin in the specific lead quantization axis (different, in general, from the one of the system). The annihilation operator $\hat{c}_b$ destroys the lead electron with the corresponding energy ε_b. We assume for the leads, in the spirit of the Stoner model for itinerant ferromagnets, a spin-dependent dispersion relation $\varepsilon_{l\boldsymbol{k}\uparrow_l} \neq \varepsilon_{l\boldsymbol{k}\downarrow_l}$, yielding a different density of states at the Fermi energy $g_{l\sigma_l}(E_\mathrm{F})$ for the majority and minority spin states. The spin polarization for the lead l is thus obtained as

$$P^l_\mathrm{s} = \frac{g_{l\uparrow_l}(E_\mathrm{F}) - g_{l\downarrow_l}(E_\mathrm{F})}{g_{l\uparrow_l}(E_\mathrm{F}) + g_{l\downarrow_l}(E_\mathrm{F})}. \quad (8)$$

The leads are kept at the same temperature T, with the electrochemical potentials μ_l modulated by the external bias $\mu_\mathrm{L,R} = \pm eV_\mathrm{b}/2$.

The tunneling Hamiltonian

$$\hat{H}_\mathrm{tun} = \sum_{bi\sigma} t_{b,i\sigma}\,\hat{c}^\dagger_b\,\hat{d}_{i\sigma} + t^*_{b,i\sigma}\,\hat{d}^\dagger_{i\sigma}\,\hat{c}_b \quad (9)$$

combines via the tunneling amplitudes $t_{b,i\sigma}$ the operators of the leads with the four system operators $\{\hat{d}_{\mathrm{T}\uparrow}, \hat{d}_{\mathrm{B}\uparrow}, \hat{d}_{\mathrm{T}\downarrow}, \hat{d}_{\mathrm{B}\downarrow}\}$. The tunneling amplitudes incorporate several aspects of the tunneling process, related to the specific geometry of the tunnel barrier. For systems with negligible intrinsic SOI and very localized dot-wave functions, the tunneling amplitudes $t_{l\boldsymbol{k}\sigma_l,i\sigma}$ can be factorized into a spin and an orbital overlap:

$$t_{l\boldsymbol{k}\sigma_l,i\sigma} \approx \varepsilon_0\langle l\boldsymbol{k}\sigma_l|i\sigma\rangle = \varepsilon_0\langle l\boldsymbol{k}|i\rangle\langle\sigma_l|\sigma\rangle. \quad (10)$$

The explicit derivation of the tunneling amplitudes for a specific microscopic model is given in Appendix A 1.

The calculation of the CST dynamics of a system with a quasidegenerate many-body spectrum requires the evaluation of the tunneling rate matrices [28,29]. The latter are deduced from $\hat{H}_{\rm tun}$ and are defined on the single-particle space of the system as

$$\Gamma^l_{i\sigma,j\sigma'}(E) = \frac{2\pi}{\hbar}\sum_{\boldsymbol{k}\sigma_l} t^*_{l\boldsymbol{k}\sigma_l,i\sigma}\, t_{l\boldsymbol{k}\sigma_l,j\sigma'}\, \delta(E-\varepsilon_{l\boldsymbol{k}\sigma_l}). \tag{11}$$

To proceed further in the analysis of the tunneling rate matrices, we also assume the density of states for both spin species to be rather smooth in the vicinity of the Fermi level. We thus introduce the approximation

$$\delta(E-\varepsilon_{l\boldsymbol{k}\sigma_l}) \approx \frac{g_{l\sigma_l}(E_{\rm F})}{g_{l\uparrow_l}(E_{\rm F})+g_{l\downarrow_l}(E_{\rm F})}\sum_{\tau_l}\delta(E-\varepsilon_{l\boldsymbol{k}\tau_l}). \tag{12}$$

The sum over the lead spin index τ_l compensates, in the limit $E\to E_{\rm F}$, the denominator, and Eq. (12), integrated on the momenta $\boldsymbol{k}$, becomes exact.

By combining Eqs. (10)–(12), we obtain a tunneling rate matrix of the form

$$\Gamma^l_{i\sigma,j\sigma'}(E) = \frac{2\pi}{\hbar}\varepsilon_0^2\sum_{\boldsymbol{k}}\langle i|l\boldsymbol{k}\rangle\langle l\boldsymbol{k}|j\rangle\sum_{\tau_l}\delta(E-\varepsilon_{l\boldsymbol{k}\tau_l}) \times\sum_{\sigma_l}\frac{g_{l\sigma_l}(E_{\rm F})}{g_{l\uparrow_l}(E_{\rm F})+g_{l\downarrow_l}(E_{\rm F})}\langle\sigma|\sigma_l\rangle\langle\sigma_l|\sigma'\rangle, \tag{13}$$

which can be factorized into a bare tunneling rate, an orbital and a spin component

$$\Gamma^l = \Gamma^l_0 A^l\otimes B^l, \tag{14}$$

where we omit, for simplicity, the energy dependence. The bare tunneling rate Γ^l_0, and the generic elements of the orbital A^l_{ij} and of the spin matrix $B^l_{\sigma\sigma'}$, are defined in terms of the wave function overlaps and single-particle spectra:

$$\Gamma^l_0 = \frac{2\pi}{\hbar}\varepsilon_0^2\sum_{i\boldsymbol{k}\sigma_l}|\langle i|l\boldsymbol{k}\rangle|^2\delta(E-\varepsilon_{l\boldsymbol{k}\sigma_l}), \tag{15}$$

$$A^l_{ij} = \frac{\sum_{\boldsymbol{k}\sigma_l}\langle i|l\boldsymbol{k}\rangle\langle l\boldsymbol{k}|j\rangle\delta(E-\varepsilon_{l\boldsymbol{k}\sigma_l})}{\sum_{a\boldsymbol{q}\tau_l}|\langle a|l\boldsymbol{q}\rangle|^2\delta(E-\varepsilon_{l\boldsymbol{q}\tau_l})}, \tag{16}$$

$$B^l_{\sigma\sigma'} = \sum_{\sigma_l}\frac{g_{l\sigma_l}(E_{\rm F})}{g_{l\uparrow_l}(E_{\rm F})+g_{l\downarrow_l}(E_{\rm F})}\langle\sigma|\sigma_l\rangle\langle\sigma_l|\sigma'\rangle. \tag{17}$$

Since both A^l and B^l are Hermitian 2×2 matrices of trace 1, they can be expanded in terms of Pauli matrices as

$$A^l = \left(\frac{\mathbb{1}_2}{2}+\frac{P^l_{\rm o}}{2}\boldsymbol{n}^l_{\rm o}\cdot\boldsymbol{\sigma}\right),\qquad B^l = \left(\frac{\mathbb{1}_2}{2}+\frac{P^l_{\rm s}}{2}\boldsymbol{n}^l_{\rm s}\cdot\boldsymbol{\sigma}\right), \tag{18}$$

where $P^l_{\rm s}$ is the spin polarization defined in Eq. (8), $\boldsymbol{n}^l_{\rm s}$ is the direction of the spin quantization axis for the lead l, and $\boldsymbol{\sigma}$ is the vector of the Pauli matrices. Analogously, we define $P^l_{\rm o}$ and $\boldsymbol{n}^l_{\rm o}$ as the strength and the direction of the orbital (pseudospin) polarization of the l lead.

The pseudospin polarization of the lead allows for a simple physical interpretation, in connection to the pseudospin formulation of the system Hamiltonian. Full pseudospin polarization in the z direction indicates an exclusive coupling to the top (or to the bottom) dot. Components in the x-y plane describe instead coherent tunneling of one electron to both orbitals.

It is thus understandable how such off-diagonal components of the tunneling rate matrix are necessary for the observation of interference effects. In particular, in complete analogy to the spin valve [3], tunneling is forbidden from a DQD with maximum expectation value of the pseudospin in a given direction (i.e., 1/2 for the one- and three-particle sector, 1 for the two-particle sector) and a lead fully polarized in the opposite direction. Exemplarily, a state with double occupation of the top dot cannot release any electron to a lead which only couples to the bottom dot. The pseudospin formulation allows us to capture on an equal footing also the other polarization direction which, on the contrary, is not so easily described within the position representation.

In the following, we choose parallel spin and almost antiparallel pseudospin directions:

$$\boldsymbol{n}^{\rm L,R}_{\rm o} = \left(\cos\frac{\theta}{2}, 0, \mp\sin\frac{\theta}{2}\right) \tag{19}$$

with the opening angle $\theta = 0.95\pi$ (cf. Fig. 1). Moreover, we will always use equal spin (orbital) polarization for both leads in our calculations ($P_{\rm s}=P^{\rm L}_{\rm s}=P^{\rm R}_{\rm s}$ and $P_{\rm o}=P^{\rm L}_{\rm o}=P^{\rm R}_{\rm o}$). Furthermore, we assume that the axis of the lead spin σ_l and the one of the system σ coincide so that we switch to σ as the overall spin index. Finally, we consider high pseudospin polarizations ($P_{\rm o}\approx 1$) to achieve an essentially closed pseudospin valve [11].

A concrete example of pseudospin description is given in [25]. The angular momentum states of the CNT provide a two-level system with symmetry-protected degeneracy. The pseudospin polarization of the leads is there related to the extent and position of the contact region between the lead and the CNT. The localized contact provides an almost full polarization. The control of the phase and strength of the tunneling amplitudes can be achieved with the help of a longitudinal magnetic field acting on the CNT, as recently proved in [30].

In Appendix A 1, we propose instead a microscopic model based on the DQD geometry of Fig. 1. We explicitly relate the position of the dots to the parametrization of the tunneling rate matrices components A^l and B^l and thus reproduce the desired pseudospin valve parameters Γ^l_0, $P_{\rm o}$, and θ. The specific setup chosen in this paper would then correspond to a situation where the left (right) lead is primarily coupled to the bottom (top) dot. Additionally, the opening angle $\theta\lesssim\pi$ accounts for a small component of coherent, simultaneous tunneling through both dots.

Finally, it is interesting to notice how an asymmetry in the on-site energy of the DQD as well as a top-bottom tunneling amplitude t in the Hamiltonian could be seen in the framework of pseudospin as a pseudo-magnetic-field:

$$\hat{H}_{\rm DQD} = \left(\bar{\varepsilon}-\frac{U}{2}\right)\hat{N}+\frac{U+V}{4}\hat{N}^2+(U-V)\hat{T}_z^2+\boldsymbol{B}_{\rm o}\cdot\hat{\boldsymbol{T}} \tag{20}$$

with $\bar{\varepsilon} = (\varepsilon_T + \varepsilon_B)/2 + eV_g$, $B_{o,x} = 2\mathrm{Re}\, t$, $B_{o,y} = 2\mathrm{Im}\, t$, and $B_{o,z} = \Delta\varepsilon = \varepsilon_T - \varepsilon_B$. The tunneling and the orbital asymmetry would lift the orbital degeneracy of our system and thus destroy the pseudospin resonances if the magnitude of such Zeeman-like splitting is big enough. We argue that a small hopping and asymmetry $|t|, \Delta\varepsilon < \hbar\Gamma_0$ are not detrimental as the coupling to the leads Γ_0 cannot resolve the lifted degeneracies. Therefore, one still expects interference effects to appear. The pseudo-magnetic-field $\boldsymbol{B}_o$ would simply add to the exchange one, that, as explained in the next section, is generated by the virtual electron fluctuations between the DQD and the leads.

III. TRANSPORT THEORY

We calculate the transport characteristics following two complementary approaches. On the one side, we derive a generalized master equation (GME) for the reduced density matrix in a next to leading order expansion in the tunneling coupling. We then evaluate the steady state current and differential conductance by numerical integration of the GME.

On the other side, in the appropriate range of parameters, we deduce from the GME a minimal set of coupled rate equations involving a small number of relevant observables (i.e., the occupation probabilities of the empty and singly occupied DQD supplemented by the spin-resolved components of the pseudospin vector). The analytical solution of such equations allows us for a clear interpretation of the numerical results in terms of CST dynamics.

A. Generalized master equation

The starting point for the derivation of a GME is the Liouville–von Neumann equation. The latter can be formulated in terms of the Liouville superoperator $\mathcal{L}$

$$\dot{\hat{\rho}}(t) = -\frac{i}{\hbar}[\hat{H}, \hat{\rho}] =: \mathcal{L}\hat{\rho}(t), \tag{21}$$

where $\hat{H}$ is the Hamiltonian in Eq. (1) and $\dot{\hat{\rho}}(t)$ is the time derivative of the density matrix for the full system-bath model. The Liouville superoperator is a linear operator acting on the vector space of the Hermitian operators, themselves defined on the Fock space of the system-bath model.

The aim of the GME is to focus on the dynamics of the system. We thus integrate Eq. (21) over the leads' degrees of freedom and obtain an equation of motion for the reduced density matrix $\hat{\rho}_{\mathrm{red}} = \mathrm{Tr}_{\mathrm{leads}}\{\hat{\rho}\}$. The GME, as compared to the Pauli master equation, also retains the dynamics of the coherences (i.e., the off-diagonal terms) of $\hat{\rho}_{\mathrm{red}}$. This approach is necessary for systems exhibiting a degenerate spectrum and it allows us to capture interference effects even in interacting systems weakly coupled to leads [3,6,15,24,25].

To this end, it is useful to split the full Liouvillian $\mathcal{L}$ into the sum of three terms $\mathcal{L} = \mathcal{L}_{\mathrm{leads}} + \mathcal{L}_{\mathrm{DQD}} + \mathcal{L}_{\mathrm{tun}}$ each indicating, in analogy to Eq. (21), the commutator with the corresponding component of the Hamiltonian in Eq. (1). The equation of motion for $\hat{\rho}_{\mathrm{red}}$ is deduced within a perturbative scheme for the tunneling Liouvillian $\mathcal{L}_{\mathrm{tun}}$. The method of choice to derive a GME is the Nakajima-Zwanzig projection operator technique [31,32]. The main idea behind this approach consists of splitting the total density operator into two components: one in which the QD system and the leads are separated ($\mathcal{P}\hat{\rho}$) and the other in which, on the contrary, the entanglement of the QD system and the leads is captured ($\mathcal{Q}\hat{\rho}$). The projectors extracting these two components are defined as $\mathcal{P} = \mathrm{Tr}_{\mathrm{leads}}\{\bullet\} \otimes \hat{\rho}_{\mathrm{leads}}$ and $\mathcal{Q} = 1 - \mathcal{P}$, where $\hat{\rho}_{\mathrm{leads}}$ is the reference equilibrium density matrix of the leads.

The Liouville–von Neumann equation transforms into a set of coupled equation for the factorized and the nonfactorized components, respectively $\mathcal{P}\hat{\rho}$ and $\mathcal{Q}\hat{\rho}$. By formally solving the equation for $\mathcal{Q}\hat{\rho}$ and inserting the result into the equation for $\mathcal{P}\hat{\rho}$, one obtains the Nakajima-Zwanzig equation for the factorized component of the density operator $\mathcal{P}\hat{\rho}$ [33]:

$$\mathcal{P}\dot{\hat{\rho}}(t) = \mathcal{L}_{\mathrm{DQD}}\mathcal{P}\hat{\rho}(t) + \int_0^t ds\, \mathcal{K}(t-s)\mathcal{P}\hat{\rho}(s) \tag{22}$$

with the kernel superoperator

$$\mathcal{K}(t) = \mathcal{P}\mathcal{L}_{\mathrm{tun}}\bar{\mathcal{G}}_{\mathcal{Q}}(t)\mathcal{L}_{\mathrm{tun}}\mathcal{P} \tag{23}$$

containing the propagator for the entangled part $\bar{\mathcal{G}}_{\mathcal{Q}}(t)$ defined as

$$\bar{\mathcal{G}}_{\mathcal{Q}}(t) = e^{(\mathcal{L}_{\mathrm{DQD}} + \mathcal{L}_{\mathrm{leads}} + \mathcal{Q}\mathcal{L}_{\mathrm{tun}}\mathcal{Q})t}. \tag{24}$$

A final, formally trivial, trace over the leads of Eq. (22) yields the desired equation of motion for the reduced density operator.

Equation (22) is still exact since it contains all orders in the tunneling Liouvillian $\mathcal{L}_{\mathrm{tun}}$ as it is easily verified by inspection of Eq. (24). Moreover, Eq. (22) also captures memory effects, as the dynamics of the reduced density matrix at time t depends on the state of the system at all previous times. In the present work, we concentrate, though, only on the steady state of the system, defined as $\hat{\rho}^{\infty}_{\mathrm{red}} := \mathrm{Tr}_{\mathrm{leads}}\{\hat{\rho}(t \to \infty)\}$.

With the help of the Laplace transformation, the convolutive form of the kernel, and the final value theorem, we obtain the following equation for the stationary reduced density operator [34–37]:

$$\mathrm{Tr}_{\mathrm{leads}}\left\{(\mathcal{L}_{\mathrm{DQD}} + \tilde{\mathcal{K}})\hat{\rho}^{\infty}_{\mathrm{red}} \otimes \hat{\rho}_{\mathrm{leads}}\right\} = 0 \tag{25}$$

with

$$\tilde{\mathcal{K}} = \mathcal{P}\mathcal{L}_{\mathrm{tun}} \sum_{n=0}^{\infty} (\tilde{\mathcal{G}}_0 \mathcal{Q}\mathcal{L}_{\mathrm{tun}}\mathcal{Q})^{2n}\tilde{\mathcal{G}}_0\mathcal{L}_{\mathrm{tun}}\mathcal{P}, \tag{26}$$

where

$$\tilde{\mathcal{G}}_0 = \lim_{\lambda \to 0^+} \frac{1}{\lambda - \mathcal{L}_{\mathrm{DQD}} - \mathcal{L}_{\mathrm{leads}}} \tag{27}$$

is the Laplace transform of the free propagator, for the DQD and the leads, in the absence of tunneling coupling. The tunneling Hamiltonian does not conserve the leads' particle number, $\mathcal{P}\mathcal{L}_{\mathrm{tun}}^{2n+1}\mathcal{P} = 0$ for $n \in \mathbb{N}$; i.e., only an even number of $\mathcal{L}_{\mathrm{tun}}$ survives the trace over the bath degrees of freedom in Eq. (26).

The Laplace transform of the propagation kernel calculated at $\lambda \to 0$ also serves for the formulation of the Markovian limit of the GME:

$$\mathcal{P}\dot{\hat{\rho}}(t) = (\mathcal{L}_{\mathrm{DQD}} + \tilde{\mathcal{K}})\mathcal{P}\hat{\rho}(t). \tag{28}$$

Differently from Eq. (22), this equation is local in time. Consequently, it does not contain memory effects and its

derivation is only justified if the timescale of the evolution of the reduced density matrix is much longer than the decay time of the propagation kernel $\mathcal{K}(t-s)$ and, ultimately, of the bath correlator functions [33].

For sufficiently small coupling to the leads ($\hbar\Gamma_0 \ll U, k_BT$) also a perturbative expansion of the propagation kernel in Eq. (26) in the tunneling Liouvillian is justified. The first term of the sum in Eq. (26) reproduces the CST regime

$$\tilde{\mathcal{K}}^{(2)} = \mathcal{P}\mathcal{L}_{\rm tun}\tilde{\mathcal{G}}_0\mathcal{L}_{\rm tun}\mathcal{P}. \tag{29}$$

We consider here a truncation up to the next order, i.e., the cotunneling regime: $\tilde{\mathcal{K}} \approx \tilde{\mathcal{K}}^{(2)} + \tilde{\mathcal{K}}^{(4)}$. From Eq. (26), we obtain

$$\begin{aligned}\tilde{\mathcal{K}}^{(4)} = {}& \mathcal{P}\mathcal{L}_{\rm tun}\tilde{\mathcal{G}}_0\mathcal{L}_{\rm tun}\tilde{\mathcal{G}}_0\mathcal{L}_{\rm tun}\tilde{\mathcal{G}}_0\mathcal{L}_{\rm tun}\mathcal{P} \\ & - \mathcal{P}\mathcal{L}_{\rm tun}\tilde{\mathcal{G}}_0\mathcal{L}_{\rm tun}\mathcal{P}\tilde{\mathcal{G}}_0\mathcal{P}\mathcal{L}_{\rm tun}\tilde{\mathcal{G}}_0\mathcal{L}_{\rm tun}\mathcal{P},\end{aligned} \tag{30}$$

where the second term compensates the reducible Wick's contraction still contained in the first one [34]. A more detailed evaluation for the CST and the cotunneling kernels is given in Appendix A 2.

Any stationary expectation value of a system observable can be obtained as $O = \mathrm{Tr}_{\rm DQD}\{\hat{O}\hat{\rho}^{\infty}_{\rm red}\}$. Moreover, from the stationary density matrix $\hat{\rho}^{\infty}_{\rm red}$, also the stationary current at lead l is evaluated,

$$I_l = \mathrm{Tr}_{\rm DQD+leads}\left\{\mathcal{K}_{I_l}\hat{\rho}^{\infty}_{\rm red}\otimes\hat{\rho}_{\rm leads}\right\}, \tag{31}$$

where the current kernel $\mathcal{K}_{I_l}$ is obtained from the propagator kernel in Eq. (26) by changing the leftmost tunneling Liouvillian with the current operator,

$$\hat{I}_l = \frac{ie}{\hbar}\sum_{\boldsymbol{k}\sigma_l a\sigma} t_{l\boldsymbol{k}\sigma_l,a\sigma}\,\hat{c}^{\dagger}_{l\boldsymbol{k}\sigma_l}\hat{d}_{a\sigma} - t^{*}_{l\boldsymbol{k}\sigma_l,a\sigma}\,\hat{d}^{\dagger}_{a\sigma}\hat{c}_{l\boldsymbol{k}\sigma_l}, \tag{32}$$

where e is the electronic charge.

Consistently, the same order in the perturbative expansion has been kept in the propagator as well as in the current kernel. With the help of a treatment of the cotunneling integrals (cf. Appendix A 2) founded on the work of [34–36,38,39], we have implemented a transport code which includes all coherences necessary to capture the interference effects in our system. Moreover, the next to leading order expansion allowed for a systematic test of robustness of the interference effects beyond the CST approximation.

B. Minimal rate model

In order to gain a clearer physical understanding of the numerical results, we also set up a minimal model in the CST regime [27]. To this purpose, we start from Eq. (28) and retain only the CST kernel $\tilde{\mathcal{K}}^{(2)}$ given in Eq. (29). The equation of motion for the reduced density operator can be cast into the simple form

$$\dot{\hat{\rho}}_{\rm red} = -\frac{i}{\hbar}[\hat{H}_{\rm DQD} + \hat{H}_{\rm LS}, \hat{\rho}_{\rm red}] + \mathcal{L}_{\rm T}\hat{\rho}_{\rm red}, \tag{33}$$

where $\mathcal{L}_{\rm T}$ describes the tunneling events among many-body states with consecutive particle numbers and $\hat{H}_{\rm LS}$ is the Lamb shift Hamiltonian, which renormalizes the coherent DQD dynamics and is due to virtual charge fluctuations [20]. A detailed derivation of Eq. (33) is given in Appendices A 2 and A 3.

We observe that, in general, Eq. (33) would yield, for the system at hand, a set of 256 coupled equations for the different matrix elements of $\hat{\rho}_{\rm red}$ calculated in an arbitrary many-body basis. As we focus our interest on gate and bias voltages corresponding to at most one particle in the DQD, we restrict ourselves to the coupled dynamics of the populations p_0 and p_σ (empty and singly occupied DQD with spin σ) complemented each by one of the spin-resolved pseudospin vectors $\boldsymbol{T}_\sigma$. These observables are obtained as the expectation values of system operators:

$$p_0 = \langle\hat{P}_0\rangle, \quad p_\sigma = \langle\hat{P}_\sigma\rangle, \quad T_{\sigma,\alpha} = \langle\hat{P}_\sigma\hat{T}_\alpha\hat{P}_\sigma\rangle, \tag{34}$$

where $\langle\bullet\rangle = \mathrm{Tr}_{\rm DQD}\{\hat{\rho}_{\rm red}\bullet\}$, $\hat{P}_0 = |\emptyset\rangle\langle\emptyset|$ is the projector on the empty state, $\hat{P}_\sigma = \sum_i \hat{d}^{\dagger}_{i\sigma}\hat{P}_0\hat{d}_{i\sigma}$, and $\hat{T}_\alpha$ is the $\alpha = x, y, z$ component of the pseudospin operator defined in Eq. (3).

Due to the conservation of the particle number and z component of the spin for parallel polarized leads, in the range of bias and gate voltages relevant for our considerations, the reduced density matrix is block diagonal and can be approximated with the expression

$$\rho_{\rm red} \approx p_0 \oplus \left(\frac{p_\uparrow}{2}\mathbb{1}_2 + \boldsymbol{T}_\uparrow\cdot\boldsymbol{\sigma}\right) \oplus \left(\frac{p_\downarrow}{2}\mathbb{1}_2 + \boldsymbol{T}_\downarrow\cdot\boldsymbol{\sigma}\right), \tag{35}$$

where $\oplus$ denotes a direct sum. By inserting Eq. (35) into Eq. (28) with the kernel evaluated in the CST limit, we compute the time derivatives of the expectation values of Eq. (34). In analogy to the spin valve case discussed in [3], the following set of coupled Bloch-like equations can be obtained:

$$\dot{p}_0 = -4\gamma^{+}p_0 + \sum_\sigma D_\sigma(\gamma^{-}p_\sigma + 2\boldsymbol{\gamma}^{-}\cdot\boldsymbol{T}_\sigma), \tag{36}$$

$$\dot{p}_\sigma = D_\sigma(2\gamma^{+}p_0 - \gamma^{-}p_\sigma - 2\boldsymbol{\gamma}^{-}\cdot\boldsymbol{T}_\sigma), \tag{37}$$

$$\dot{\boldsymbol{T}}_\sigma = D_\sigma\left(-\gamma^{-}\boldsymbol{T}_\sigma + p_0\boldsymbol{\gamma}^{+} - \frac{p_\sigma}{2}\boldsymbol{\gamma}^{-}\right) + \boldsymbol{B}_\sigma\times\boldsymbol{T}_\sigma, \tag{38}$$

where we have introduced vector and scalar rates, respectively $\boldsymbol{\gamma}^{\pm} = \sum_l P_{\rm o}\Gamma^l_0 f^{\pm}_l(\varepsilon)\boldsymbol{n}^l_{\rm o}$ and $\gamma^{\pm} = \sum_l \Gamma^l_0 f^{\pm}_l(\varepsilon)$. Moreover, $D_{\uparrow,\downarrow} = 1 \pm P_{\rm s}$ and, for the Fermi functions, we adopt the notation $f^{\pm}_l(\varepsilon) = [e^{\pm(\varepsilon-\mu_l)/(k_BT)}+1]^{-1}$.

The conservation of probability imposes that $\dot{p}_0 + \dot{p}_\uparrow + \dot{p}_\downarrow = 0$. This relation is clearly satisfied by the differential equations (36) and (37). Besides the gain-loss relations between the populations p_0 and p_σ, they contain the terms $\pm 2D_\sigma\boldsymbol{\gamma}^{-}\cdot\boldsymbol{T}_\sigma$ which ensure the coupling of the populations to the dynamics of the spin-resolved pseudospin vectors $\boldsymbol{T}_\sigma$.

Three conceptually different mechanisms yield the time evolution of the pseudospin described by such a Bloch-like equation: the first term in Eq. (38) describes relaxation, accumulation due to the tunneling from the zero- and toward the two-particle states characterizes the following two terms. The last term contains the *spin-dependent* pseudo-exchange-field $\boldsymbol{B}_\sigma$ which, analogously to a magnetic field, generates pseudospin precession. The spin-dependent pseudo-exchange-field reads

$$\begin{aligned}\boldsymbol{B}_\sigma = {}& \sum_l 2P_{\rm o}\Gamma^l_0\big\{D_\sigma[p_l(E_{10}) - p_l(E_{2{\rm g}1})]\boldsymbol{n}^l_{\rm o} \\ & + D_{\bar{\sigma}}[p_l(E_{2{\rm e}1}) - p_l(E_{2{\rm g}1})]\big(\boldsymbol{n}^l_{\rm o}\cdot\boldsymbol{e}_z\big)\boldsymbol{e}_z\big\}\end{aligned} \tag{39}$$

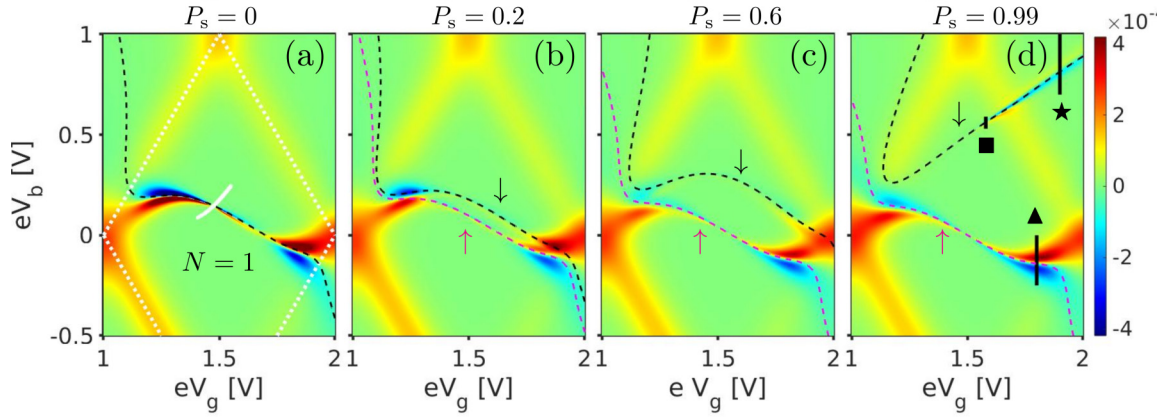

FIG. 2. Differential conductance of a DQD shows pseudospin resonances tuned by spin polarization P_s: The one-particle diamond is highlighted by the dotted white lines in panel (a). The three vertical black lines (★, ■, ▲) indicate the bias traces of Fig. 3. The dashed magenta (black) line is the resonance condition of the ↑ (↓) electrons [cf. Eq. (41)]. The solid white line indicates the minimum of $B_{\sigma,\perp}$ which matches perfectly a local minimum within the pseudospin resonance. The parameters are the following: $U = 2V$, $k_BT = 0.05V$, $P_o = 0.99$, $\theta = 0.95\pi$, $\Gamma_0^R = 2.5 \times 10^{-3}V = 2\Gamma_0^L$, $\varepsilon_0 = -2V$, and $W = 250V$ (bandwidth).

with

$$p_l(x) = \frac{1}{2\pi}\mathrm{Re}\Psi^{(0)}\left(\frac{1}{2} + i\frac{x-\mu_l}{2\pi k_BT}\right), \tag{40}$$

where $\Psi^{(0)}(z)$ is the digamma function. The subscript of the energy $E_{ss'}$ labels the energy difference between the state s and s′ which can be the zero-particle state (0), the one-particle state (1), and the two-particle excited/ground state (2e/2g).

Such a field arises due to virtual fluctuations of the system to the neighboring empty *and* doubly occupied DQD states. It is crucial to include in the exchange field the two-particle states, even though we do not account explicitly for the dynamics of their populations. Also energy levels far from the CST resonance do influence the exchange field due to the logarithmic tails of the digamma functions.

The pseudo-exchange-fields associated with the majority and the minority spins differ from each other both in strength and orientation, thus giving raise to a SOI, which, due to the complete absence of intrinsic spin-orbit in the system, we call synthetic. As will become clear in Sec. IV, such synthetic SOI determines the rich variety of phenomena decorating the first Coulomb diamond.

It is the first line in Eq. (39) which gives the most relevant contribution to $\boldsymbol{B}_\uparrow$. The second line dominates, instead, $\boldsymbol{B}_\downarrow$. Especially for leads with a very high spin polarization, we can conclude that the pseudo-exchange-field of minority spins always points approximately toward the z direction, which represents the hard axis of the pseudospin anisotropy. Instead, the majority spin field $\boldsymbol{B}_\uparrow$ oscillates, as a function of the bias and gate voltage, between the two directions $\boldsymbol{n}_o^L$ and $\boldsymbol{n}_o^R$.

Interestingly, for an isotropic system ($U = V$) the two fields would be collinear, with the difference in strength stemming merely from the different spin-resolved density of states in the leads. For normal metallic leads, the two fields even coincide. It is thus clear that only the interplay of the spin polarization in the leads and the pseudospin anisotropy can explain the synthetic SOI.

IV. RESULTS

The stability diagram, i.e., the differential conductance displayed as a function of bias and gate voltage, of a DQD in the cotunneling regime is shown, in Fig. 2, for several spin polarizations of the leads. We focus on the one-particle Coulomb diamond, highlighted in panel (a) by the dotted white lines. Here, we would normally expect a featureless exponentially suppressed differential conductance, as the consequence of an essentially fixed particle number and, due to Coulomb repulsion, a smooth, exponentially suppressed current.

Contrary to the expectations, we can clearly see in panel (a) a distinctive resonance, highlighted by the dashed black line, cutting through the Coulomb diamond. Increasing the spin polarization P_s [Figs. 2(b)–2(d)] leads to a splitting of this resonance, marked by the dashed lines. In the upper right corner of Fig. 2(d), a resonance can be observed even outside the diamond. Although introduced as current resonances, the aforementioned transport features are more visible in the differential conductance. The latter enhances, in fact, sharp current modulations within the generally suppressed Coulomb diamond background.

We rationalize those transport effects in terms of pseudospin resonances, in analogy to the spin resonances reported in [11]. The pseudospin is associated with the orbital degree of freedom of the DQD. In our setup, the orbital polarizations of the leads are almost antiparallel thus resulting in an almost closed pseudospin valve. The latter is indicated in Fig. 1 by the different sizes of the arrows connecting the leads and the dots. Solely varying the coupling strength would correspond to a sweep of the lead polarization along the z direction.

Pseudospin resonances require, instead, noncollinear orbital polarizations as well as an asymmetry in the bare coupling strength Γ_0^l between the right and left lead. The latter shifts the resonance away from the zero bias line [11]. The necessary σ^x or, equivalently, σ^y orbital polarization of the leads translates into nondiagonal Γ^l matrices, as seen in Eqs. (11) and (18), which can be interpreted as tunneling to a coherent superposition of two different orbitals. Experimental

evidence of such coherent superpositions for QDs in the weak tunneling regime has been reported in [14,25].

In the framework of Eqs. (36)–(38), vectorial resonance conditions can be formulated similarly to the ansatz in [11,27]:

$$\boldsymbol{B}_\sigma \cdot \left(\boldsymbol{n}_\mathrm{o}^\mathrm{L} - \boldsymbol{n}_\mathrm{o}^\mathrm{R}\right) = 0. \tag{41}$$

The spin-dependent exchange field generates two distinct conditions, each determining the position of the corresponding resonance in the V_g-V_b plane: the magenta (black) dashed line in Fig. 2 for the ↑ (↓) electrons. The accuracy of Eq. (41) in determining the resonance positions reduces as the angle θ is chosen farther away from antiparallel alignment. In contrast to the resonance conditions formulated in [11] and in [27], we choose Eq. (41), where the drain and the source equally participate, since it matches the numerical resonances on a broader parameter range.

Despite the subtle differences, though, all three conditions mentioned above can only predict the *position* of the resonances, but not their *character*. The same resonance condition corresponds to a dip in the current (★ in Fig. 2), or to a peak (▲) and even to a Fano-like asymmetric peak-dip (■). Finally, the current peak is strongly modulated along the same resonance line and it can even disappear, as exemplarily highlighted in panel (a) of Fig. 2 with the solid white line. The discovery and explanation of such *qualitative* differences in the pseudospin resonances, which originate from the intertwining of spin and pseudospin, represent the main result presented in this publication.

As a first step in the analytical understanding of the rich variety of transport phenomena illustrated in Fig. 2, we calculate the stationary current in the CST limit. The current through the DQD can be expressed as the charge variation due to the coupling to a specific lead. From Eq. (37), we readily obtain

$$I_\mathrm{L} = 4\gamma_\mathrm{L}^+ p_0 - \sum_\sigma D_\sigma(\gamma_\mathrm{L}^- p_\sigma + 2\boldsymbol{\gamma}_\mathrm{L}^- \cdot \boldsymbol{T}_\sigma), \tag{42}$$

where the vector and scalar rates for the left lead read, respectively, $\boldsymbol{\gamma}_\mathrm{L}^- = \Gamma_0^\mathrm{L} P_\mathrm{o} f_\mathrm{L}^-(\varepsilon)\boldsymbol{n}_\mathrm{o}^\mathrm{L}$ and $\gamma_\mathrm{L}^\pm = \Gamma_\mathrm{L}^0 f_\mathrm{L}^\pm(\varepsilon)$. The stationary current is obtained by inserting in Eq. (42) the populations p_0^∞, p_σ^∞, and $\boldsymbol{T}_\sigma^\infty$, i.e., the stationary solutions of Eqs. (36)–(38).

Panels (a), (c), and (e) of Fig. 3 show a direct comparison between the absolute value of the current as obtained from the full numerical calculation (orange) and the analytical approach (blue) of Eq. (42). In all three cases, the analytical result well reproduces the qualitative behavior of the current and the position of its extrema.

For a deeper understanding of the resonances of Figs. 2 and 3, we further elaborate on the equations of motion, Eqs. (36)–(38). To this end, we solve Eq. (38) in the stationary limit and obtain, for the accumulated pseudospin,

$$\boldsymbol{T}_\sigma^\infty = \boldsymbol{F}_\sigma(\boldsymbol{b}_\sigma), \tag{43}$$

where we introduced the auxiliary function

$$\boldsymbol{F}_\sigma(\boldsymbol{x}) = \frac{a_\sigma}{a_\sigma^2 + |\boldsymbol{B}_\sigma|^2}\left(\boldsymbol{x} + \frac{\boldsymbol{B}_\sigma \cdot \boldsymbol{x}}{a_\sigma^2}\boldsymbol{B}_\sigma + \frac{\boldsymbol{B}_\sigma \times \boldsymbol{x}}{a_\sigma}\right) \tag{44}$$

with $a_\sigma = D_\sigma \gamma^-$, together with the vector $\boldsymbol{b}_\sigma = D_\sigma(p_0\boldsymbol{\gamma}^+ - p_\sigma\boldsymbol{\gamma}^-/2)$.

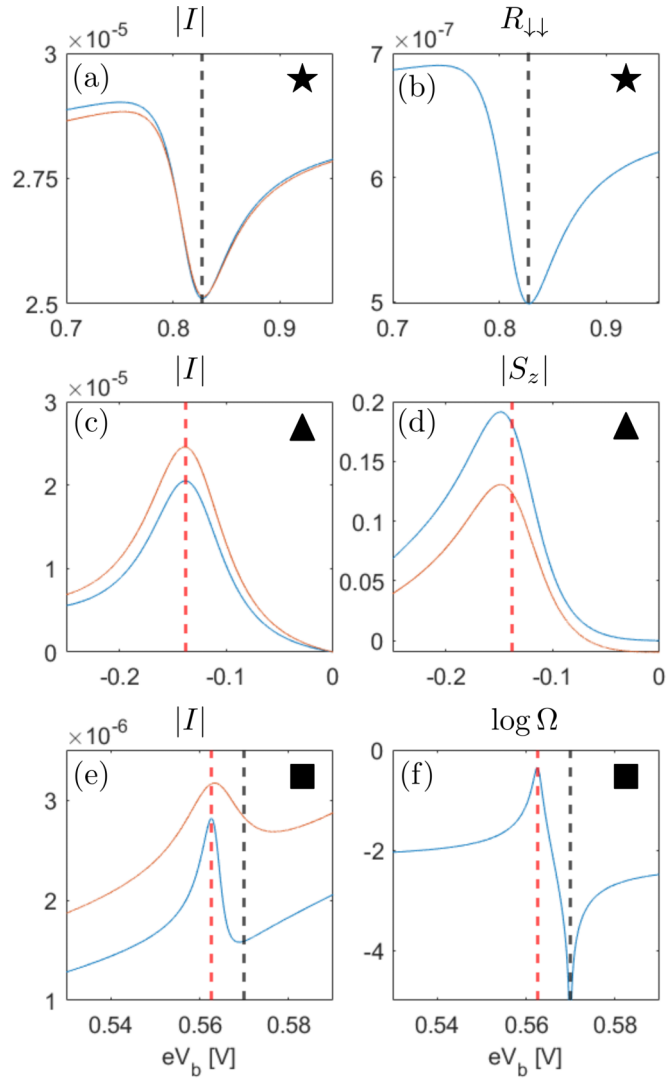

FIG. 3. Effective rate analysis of the bias traces from Fig. 2(d): The absolute value of the current shows (a) a dip at $eV_\mathrm{g} = 1.9V$, (c) a peak at $eV_\mathrm{g} = 1.8V$, and (e) a Fano-like shape at $eV_\mathrm{g} = 1.58V$. The analytic solution of the effective CST model is depicted in blue whereas the orange line shows the full cotunneling calculations. The black (red) dashed lines indicate the position of the minimum of $B_{\sigma,\perp}$ ($B_{\sigma,\parallel}$) and correspond to a minimum (maximum) of the current. (b) The rate $R_{\downarrow\downarrow}$ strongly correlates to the current. (d) The absolute value of the z component of the spin of our system $|S_z|$ is following the trend of the current. (f) The logarithm of base 10 of the ratio $\Omega = B_{\downarrow,\perp}^2/(a_\downarrow^2 + B_{\downarrow,\parallel}^2)$ highlights the two extrema of Ω that result in a peak and a dip in the current.

By substituting $\boldsymbol{T}_\sigma^\infty$ into Eqs. (36) and (37), we obtain a set of effective rate equations for the populations p_0 and p_σ:

$$\begin{pmatrix}\dot{p}_0\\ \dot{p}_\uparrow\\ \dot{p}_\downarrow\end{pmatrix} = \begin{pmatrix}-R_{00} & R_{0\uparrow} & R_{0\downarrow}\\ R_{\uparrow 0} & -R_{\uparrow\uparrow} & 0\\ R_{\downarrow 0} & 0 & -R_{\downarrow\downarrow}\end{pmatrix}\begin{pmatrix}p_0\\ p_\uparrow\\ p_\downarrow\end{pmatrix}. \tag{45}$$

The transition rates are schematically indicated in Fig. 4 and defined as

$$R_{0\uparrow} = D_\uparrow\gamma^- - D_\uparrow^2\boldsymbol{\gamma}^- \cdot \boldsymbol{F}_\uparrow(\boldsymbol{\gamma}^-),$$
$$R_{0\downarrow} = D_\downarrow\gamma^- - D_\downarrow^2\boldsymbol{\gamma}^- \cdot \boldsymbol{F}_\downarrow(\boldsymbol{\gamma}^-),$$

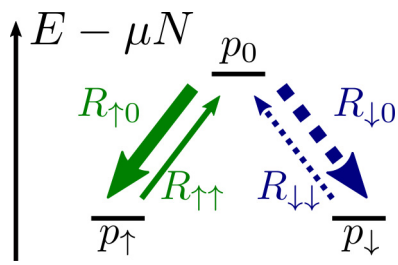

FIG. 4. Rate scheme of the three populations p_0, $p_\uparrow$, and $p_\downarrow$: The four arrows indicate the rates between the populations while their size specifies the strength of them. The dashed rates for the minority spin are furthermore lowered by the majority spin polarization of the leads.

$$R_{\uparrow 0} = 2D_\uparrow \gamma^+ - 2D_\uparrow^2 \boldsymbol{\gamma}^- \cdot \boldsymbol{F}_\uparrow(\boldsymbol{\gamma}^+),$$
$$R_{\downarrow 0} = 2D_\downarrow \gamma^+ - 2D_\downarrow^2 \boldsymbol{\gamma}^- \cdot \boldsymbol{F}_\downarrow(\boldsymbol{\gamma}^+). \tag{46}$$

Furthermore, the conservation of probability requires for the depopulation rates R_{ii} with $i = 0, \uparrow, \downarrow$

$$R_{00} = R_{\uparrow 0} + R_{\downarrow 0}, \quad R_{\sigma\sigma} = R_{0\sigma}. \tag{47}$$

In a simple physical picture, we expect a peak in the current whenever the pseudospin precession caused by the exchange field releases the blockade induced by the pseudospin valve. A dip arises, instead, whenever this mechanism is locally suppressed. Both phenomena happen in close vicinity to the aforementioned resonance condition Eq. (41). Only the analysis of the effective rates represented in Fig. 4 allows us, though, to distinguish them.

In the gate and bias voltages corresponding to the one-particle Coulomb diamond, the rates $R_{\sigma 0}$ are much larger than the depopulation rates $R_{\sigma\sigma}$. In particular, $R_{\downarrow\downarrow}$ is the smallest rate, due to the additional small density of states of the minority spins.

The current is obtained by the incoherent superposition of the minority and majority spin channels. Its modulation is thus determined, within the one-particle Coulomb diamond, by the depopulation rates $R_{\uparrow\uparrow}$ and $R_{\downarrow\downarrow}$. As confirmed by the resemblance between panels (a) and (b) in Fig. 3, the shape of a $\downarrow$ resonance is essentially given by the *bottleneck* rate

$$R_{\downarrow\downarrow} = D_\downarrow \gamma^- \left[1 - \frac{|\boldsymbol{\gamma}^-|^2}{(\gamma^-)^2} \frac{1}{1 + \frac{B_{\downarrow,\perp}^2}{a_\downarrow^2 + B_{\downarrow,\parallel}^2}} \right] \tag{48}$$

with $B_{\downarrow,\parallel}^2 = (\boldsymbol{\gamma}^- \cdot \boldsymbol{B}_\downarrow)^2 / |\boldsymbol{\gamma}^-|^2$ and $B_{\downarrow,\perp}^2 = |\boldsymbol{B}_\downarrow|^2 - B_{\downarrow,\parallel}^2$ the exchange field components parallel and perpendicular to $\boldsymbol{\gamma}^-$. In itself, $R_{\downarrow\downarrow}$ is strongly influenced by the ratio $\Omega = B_{\downarrow,\perp}^2/(a_\downarrow^2 + B_{\downarrow,\parallel}^2)$ in which the proposed physical explanation based on the precession dynamics is encoded.

In the absence of the perpendicular pseudo-magnetic-field component, no precession occurs and the bare pseudospin valve factor $|\boldsymbol{\gamma}^-|^2/(\gamma^-)^2$ reduces the rate. The other extreme is reached when the ratio Ω peaks, therefore suppressing the pseudospin valve factor. Such phenomenon only occurs if the parallel component $B_{\downarrow,\parallel}$ is minimized since the dephasing rate $a_\downarrow$ is proportional to a Fermi function, which varies smoothly within the Coulomb diamond.

The dashed lines in Fig. 3 substantiate the accuracy of the precession argument in determining the position of the current extrema. The rate $R_{\uparrow\uparrow}$, obtained by replacing $\downarrow$ with $\uparrow$ in all the elements of Eq. (48), is used for panels (c) and (d) of Fig. 3. In Fig. 3(e), both the suppression and the enhancing of the current appear in close vicinity and form a Fano-like line shape. In order to emphasize the rather weak dip, we depicted in Fig. 3(f) the logarithm of base 10 of the ratio Ω. The ratio Ω has two extrema which stem from minima of the corresponding exchange field components $B_{\downarrow,\perp}$ and $B_{\downarrow,\parallel}$. Despite its superficial resemblance to a Fano resonance, the origin of this peak-dip current resonance cannot be ascribed to the interference processes typical of Fano resonance, also seen in QD setups [40–44].

Moreover, the relevance of Ω decreases if $a_\sigma \gg |\boldsymbol{B}_\sigma|$, i.e., when the dephasing rate exceeds the precession frequency and the direction of the exchange field becomes irrelevant for the transport. Thus, no resonances appear on the left upper corner in correspondence to the black and magenta dashed lines of panels (a)–(d) of Fig. 2 even if they would be predicted by the resonance condition Eq. (41).

The analysis of the pseudospin resonances has revealed the fundamental role played by the synthetic SOI in the understanding of the transport characteristics of our system. The different orientations of the spin-resolved exchange fields explain, via Eq. (41), the splitting of the resonances. Their qualitatively different behavior as a function of the bias is rationalized instead by the depopulation rates $R_{\sigma\sigma}$ and, ultimately, again by the different orientation and strength of the pseudo-exchange-fields $\boldsymbol{B}_\sigma$.

V. CONCLUSIONS

A DQD weakly coupled to ferromagnetic leads in a pseudospin valve configuration is characterized by a rich variety of pseudospin current resonances. They decorate the Coulomb diamonds with novel features which range from a peak to a dip to a Fano shape in the current. These transport characteristics reveal the synthetic SOI induced on the system by the interplay of the spin polarization of the leads and the pseudospin anisotropy on the DQD.

Those current resonances mainly occur within the Coulomb diamond. Despite their small amplitude, they are rather sharp. Differential conductance measurements represent thus a preferential tool to highlight them, as shown in Fig. 2.

We derive the tunneling rate matrices for a microscopic model capable of reproducing the desired pseudospin polarization. To this end, we gain also physical insight into the role played by the DQD geometry in the realization of a pseudospin valve.

The cotunneling calculations ensure the robustness of the discussed effects also beyond the coherent-sequential-tunneling regime. Moreover, with the help of a minimal model, we give an accurate physical picture of the resonances and relate their position and character to a precession dynamics which modulates the pseudospin valve effect. The generality of the model allows for its applicability to the wide class of nanoscale junctions with orbital degeneracy, including, e.g., single-molecule junctions or CNT-QDs. Particularly,

coherent population trapping and signatures of pseudospin precession have been recently demonstrated in a suspended CNT quantum dot [25] with a tunneling coupling similar to the one proposed here.

The pseudospin precession underlying the rich variety of the transport phenomena highlighted in this work shall leave its fingerprints beyond the dc transport limit. To this end, we envisage, for these systems, the investigation of current noise as well as of the response to driven pump-probe protocols, which would unravel the dynamics induced by the synthetic SOI directly in the time domain.

ACKNOWLEDGMENTS

We thank M. Grifoni for fruitful discussions. The authors acknowledge moreover the financial support from the Elitenetzwerk Bayern via the IGK Topological Insulators and the Deutsche Forschungsgemeinschaft via the SFB 1277 (subprojects B02 and B04).

APPENDIX

1. Microscopic model of a pseudospin valve

In this section, we provide a microscopic model for the coupling between a DQD and ferromagnetic leads which results in the desired pseudospin valve configuration. The wave functions of the leads and of the dots are defined in real space as

$$\Psi_{l\boldsymbol{k}}(\boldsymbol{r})\delta_{\tau\sigma_l} = \langle \boldsymbol{r}\tau|l\boldsymbol{k}\sigma_l\rangle \quad \text{and} \quad \phi_i(\boldsymbol{r})\delta_{\tau\sigma} = \langle \boldsymbol{r}\tau|i\sigma\rangle. \tag{A1}$$

If we assume the same spin quantization axis for the lead and dot, the tunneling amplitude reads, accordingly,

$$t_{l\boldsymbol{k}\sigma,i\sigma'} = \int d\boldsymbol{r}\Psi^*_{l\boldsymbol{k}}(\boldsymbol{r})\Big[-\frac{\hbar^2\nabla^2}{2m_{\rm el}} + v_{\rm DQD}(\boldsymbol{r}) + v_{\rm leads}(\boldsymbol{r})\Big]\phi_i(\boldsymbol{r})\delta_{\sigma\sigma'} \approx \varepsilon_i \int d\boldsymbol{r}\Psi^*_{l\boldsymbol{k}}(\boldsymbol{r})\phi_i(\boldsymbol{r})\delta_{\sigma\sigma'}, \tag{A2}$$

where, due to the strong localization of the system wave function, we neglect, in the approximation, the contribution of the leads' potential and ε_i is the energy of the localized dot state.

The lead wave function is parametrized, in the tunneling barrier separating the leads from the dots, in terms of k_y and k_z, the components of the momentum parallel to the lead surface, and κ, the inverse penetration length inside tunneling barrier:

$$\Psi_{l\boldsymbol{k}}(\boldsymbol{r}) = \Psi^{\perp}_{l\kappa}(x)\Psi^{\parallel}_{lk_yk_z}(y,z) = \frac{e^{-\kappa x + i(k_y y + k_z z)}}{\sqrt{SL_x}}, \tag{A3}$$

where L_x and S are, respectively, the width of the well and the area of the lead surface perpendicular to the transport direction. Along this direction the wave function decays exponentially. It is useful, for the following, to express the inverse penetration length κ in terms of the electron energy $E_{\rm el}$ and the parallel momenta k_y and k_z:

$$\kappa = \sqrt{k_y^2 + k_z^2 - \frac{2m_{\rm el}}{\hbar^2}E_{\rm el}}, \tag{A4}$$

where $m_{\rm el}$ is the (effective) electronic mass.

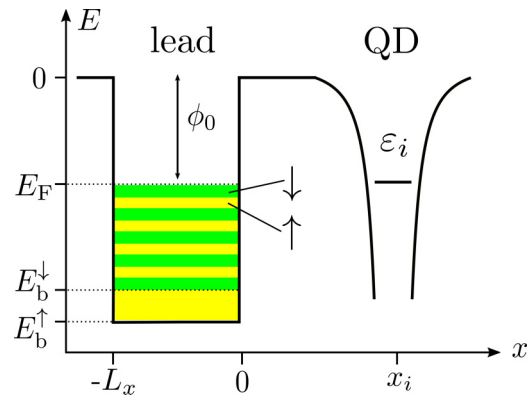

FIG. 5. Potential landscape of a lead coupled to a QD: The lead is modeled as a (large) rectangular potential well of width L_x and is separated by a distance x_i from the QD. The work function of the lead is denoted by ϕ_0 and the Fermi energy by $E_{\rm F}$. The color coding emphasizes that the bottom energy $E_{\rm b}^{\sigma}$ is bigger in its absolute value for ↑ electrons than for ↓ electrons.

The potential landscape for one lead and one QD is sketched in Fig. 5 and confines the electrons only along the x direction. The bottom energy of the rectangular potential well $E_{\rm b}^{\sigma}$ is spin dependent and the Fermi energy $E_{\rm F}$ is separated from the vacuum energy ($E = 0$) by the work function of the metal ϕ_0 [45].

With this ansatz, made in the spirit of the Stoner model for itinerant ferromagnets, we assure a different density of states at the Fermi energy for the different spin species, and obtain the desired spin polarization.

The two QD's are at distances $x_{\rm T}^l$ and $x_{\rm B}^l$ from the surface of the lead l and they feature localized bound states which we model as δ peaks centered at the position $\boldsymbol{R}_i$ of the dot. The tunneling amplitude gets thus further simplified:

$$t_{l\boldsymbol{k}\sigma,i\sigma'} = \varepsilon_i\langle l\boldsymbol{k}|i\rangle \approx \varepsilon_i \int d\boldsymbol{r}\Psi^*_{l\boldsymbol{k}}(\boldsymbol{r})a^{3/2}\delta(\boldsymbol{r}-\boldsymbol{R}_i) = \varepsilon_i a^{3/2}\Psi^*_{l\boldsymbol{k}}(\boldsymbol{R}_i) = \frac{a^{3/2}}{\sqrt{SL_x}}e^{-\kappa x_i^l - i\boldsymbol{k}_\parallel\boldsymbol{R}_i}, \tag{A5}$$

where a is a normalization factor in units of length and where we have introduced the parallel component of the momentum $\boldsymbol{k}_\parallel = (0, k_y, k_z)$.

In the following, we calculate the parameters Γ_0^l, $P_{\rm o}$, and θ starting from the definition of the tunneling rate matrix of Eq. (11). We follow two different approaches. At first, we employ the so called surface Γ-point approximation (SGPA) [46]. Subsequently, we generalize our result by taking into account the full dispersion relation of the ferromagnetic leads.

a. Surface Γ-point approximation

In a first approximation, we assume that only the state at the surface Γ point, i.e., with $k_y = k_z = 0$, participates in the transport. From Eq. (A4), we know that such a state minimizes the inverse penetration length for a fixed electronic energy and thus is expected to give the largest contribution to the tunneling. Moreover, we calculate the tunneling density matrix at the Fermi energy $E_F = -\phi_0$. Under those two conditions, the penetration length for the lead's wave function reads

$\lambda = \sqrt{\hbar^2/(2m_{\rm el}\phi_0)}$. Eventually, by inserting Eq. (A5) into the definition of the bare tunneling rate Γ_0^l of Eq. (15), we obtain

$$\tilde{\Gamma}_0^l(E_F) = \frac{2\pi}{\hbar}\frac{\varepsilon_0^2 a^3}{SL_x}\sum_\sigma g_{l\sigma}(E_{\rm F})\sum_i e^{-\frac{2x_i^l}{\lambda}}, \tag{A6}$$

where the tilde indicates the SGPA. The bare tunneling rate is thus proportional to the total density of states of the lead at the Fermi energy which scales as the volume in the thermodynamic limit and it is thus compensated by the factor SL_x at the denominator. Moreover, $\tilde{\Gamma}_0^l$ decreases exponentially upon increasing the distance between the dots and the lead. For a typical work function $\phi_0 = 5$ eV, the penetration length is approximately $\lambda = 0.9$ Å and the bare tunneling rate is reduced roughly by an order of magnitude if one increases the distance between the dots and the leads by 1 Å.

For the pseudospin component of the tunneling rate matrix, one obtains

$$\tilde{A}_{ij}^l = \frac{\exp\left(-\frac{x_i^l + x_j^l}{\lambda}\right)}{\exp\left(-\frac{2x_{\rm T}^l}{\lambda}\right) + \exp\left(-\frac{2x_{\rm B}^l}{\lambda}\right)}. \tag{A7}$$

From $\tilde{A}^l$, we can deduce the polarization angle, calculated within the same approximation:

$$\tilde{\theta}_l = \arctan\left[\sinh\left(\frac{x_{\rm B} - x_{\rm T}}{\lambda}\right)\right]. \tag{A8}$$

In our setup, we define the angle $\theta = \theta_{\rm R} - \theta_{\rm L}$ as the opening angle between the two polarization vectors. Moreover, we distribute the tilting symmetrically: $\theta_{\rm L,R} = \mp\theta/2$. Thus, an angle $\theta = 0$ corresponds to a DQD connected in parallel, with the state $|{\rm T}\rangle - |{\rm B}\rangle$ completely decoupled from both leads. Conversely, for $\theta = \pi$ the left (right) lead only couples to the bottom (top) dot, i.e., a completely closed pseudospin valve configuration.

From Eq. (A8), it is clear that the calibration of the pseudospin polarization angle requires the control of the dot position on the scale of the penetration length λ. Alternatively, one should control with local gating the barrier height and thus have access to penetration length itself.

Starting from Eq. (A7), it is straightforward to prove that, within the SGPA, the strength of the pseudospin polarization is always maximal, i.e., $\tilde{P}_{\rm o}^l = 1$. This fact is not so surprising if one considers that only the tunneling amplitude to the state at the surface Γ point is considered in the calculation of the $\tilde{A}^l$ matrix. All the other states at the Fermi energy are simply accounted for in the density of states. A more careful evaluation of the tunneling amplitudes softens the condition of full polarization. Such an evaluation offers more insight into the dependence of the pseudospin polarization strength and direction on the geometry of the junction.

b. Three-dimensional Stoner model

Relaxing the SGPA requires us to calculate the k-space integrals in Eqs. (15) and (16). The fundamental integral

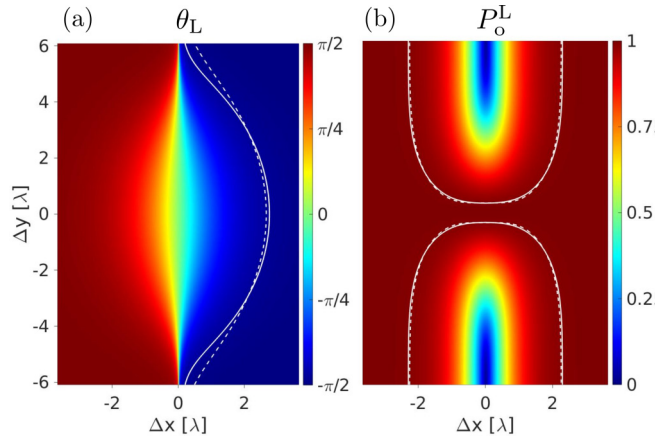

FIG. 6. Pseudospin valve parameters in variation of the relative separation of the dots exemplarily shown for the left lead: (a) The polarization angle $\theta_{\rm L}$ and (b) the polarization strength $P_{\rm o}^{\rm L}$ depend on the Δx and Δy separation of the dots. The values are obtained by a numerical integration of Eq. (A9). The parameters which are used in this publication ($P_{\rm o}^{\rm L} = 0.99$ and $\theta_{\rm L} = -0.95\pi/2$) are highlighted by the solid white lines. The dashed white lines, which coincide mostly with the solid ones, indicate the contour lines obtained by using the analytical Eqs. (A16) and (A17). The parameters are the following: $x_{\rm T}^{\rm L} + x_{\rm B}^{\rm L} = 5$ Å, $E_{\rm b}^{\uparrow} = -16.4$ eV, $E_{\rm b}^{\downarrow} = -5.0003$ eV, $\phi_0 = 5$ eV. The parameters correspond to a spin polarization of $P_{\rm s} = 0.99$.

reads

$$I_{ij} = \sum_{\boldsymbol{k}\sigma}\langle i|l\boldsymbol{k}\rangle\langle l\boldsymbol{k}|j\rangle\delta(E_{\rm F} - \varepsilon_{l\boldsymbol{k}\sigma}) = \frac{a^3 m_{\rm el}}{2\pi^2\hbar^2}\sum_\sigma\int_0^{k_{\rm F}^\sigma} dk_\parallel k_\parallel \frac{J_0[k_\parallel(y_i - y_j)]e^{-(x_i^l + x_j^l)\sqrt{\lambda^{-2} + k_\parallel^2}}}{\sqrt{\frac{2m_{\rm el}}{\hbar^2}\left(E_{\rm F} - E_{\rm b}^\sigma\right) - k_\parallel^2}}, \tag{A9}$$

where J_0 is the Bessel function of the first kind, $k_\parallel = \sqrt{k_y^2 + k_z^2}$, and the upper integration limit

$$k_{\rm F}^\sigma = \sqrt{\frac{2m_{\rm el}}{\hbar^2}\left(E_{\rm F} - E_{\rm b}^\sigma\right)} \tag{A10}$$

is the Fermi momentum for the electrons of spin σ.

On the one side, we evaluated numerically the integral in Eq. (A9), and extracted the tunneling rate parameters plotted in Fig. 6. On the other side, further insight is gained from analytical calculations carried out under specific conditions. As we are interested in a DQD in weak tunneling coupling, we assume $x_i^l + x_j^l > 3\lambda$. Moreover, we concentrate on the two limiting cases of an almost vanishing and almost full spin polarization. In the first case, we have, for a typical metallic electron density, $k_{\rm F}^\sigma \gtrsim \lambda^{-1}$, for both spin species. Thus, the numerator in Eq. (A9) is exponentially suppressed at the upper integration limit and the latter can be shifted at no price to ∞. We further neglect the $k_\parallel$ dependence in the denominator and Taylor-expand the exponent up to second order. Under these simplifications the integral can thus be solved, to give

$$I_{ij}^0 = \mathcal{C}\exp\left[-\frac{x_i^l + x_j^l}{\lambda} - \frac{(y_i - y_j)^2}{2\lambda\left(x_i^l + x_j^l\right)}\right]\left(x_i^l + x_j^l\right)^{-1} \tag{A11}$$

with

$$\mathcal{C} = \frac{2a^3 m_{\rm el}}{h^2} \sum_\sigma \left(\frac{E_{\rm b}^\sigma}{E_{\rm F}} - 1 \right)^{-\frac{1}{2}}. \tag{A12}$$

Without any loss of generality, we chose the coordinate system such that $z_{\rm T} = z_{\rm B} = 0$.

In the limit of almost full polarization, instead, $E_{\rm b}^\downarrow \approx -\phi_0$. We can thus apply the SGPA for the minority spin and obtain

$$I_{ij}^{\rm fm} = g_\uparrow(E_{\rm F}) e^{-\frac{x_i^l + x_j^l}{\lambda}} \frac{\phi_0}{E_{\rm F} - E_{\rm b}^\uparrow} \frac{\lambda}{x_i^l + x_j^l} e^{-\frac{(y_i - y_j)^2}{2\lambda(x_i^l + x_j^l)}} + g_\downarrow(E_{\rm F}) e^{-\frac{x_i^l - x_j^l}{\lambda}}, \tag{A13}$$

where

$$g_\sigma(E_{\rm F}) = \frac{1}{4\pi^2} \left(\frac{2m_{\rm el}}{\hbar^2} \right)^{3/2} \sqrt{E_{\rm F} - E_{\rm b}^\sigma}. \tag{A14}$$

With the help of Eq. (A11) or Eq. (A13), we calculate the bare tunneling coupling Γ_0^l at the Fermi energy and compare it to the one obtained in the SGPA. One obtains in both cases a reduction of the bare tunneling rate with the ratio being proportional to $(2\lambda)/(x_{\rm T}^l + x_{\rm B}^l) < 1$ in the range of validity of our analysis. The SGPA yields an upper limit for the bare tunneling strength as the tunneling amplitude is smaller for states with finite $\mathbf{k}_\parallel$ in comparison to the one at the Γ point.

Finally, the generic element of the pseudospin matrix reads, independently of the spin polarization,

$$A_{ij}^l(E_{\rm F}) = \frac{\exp\left[-\frac{x_i^l + x_j^l}{\lambda} - \frac{(y_i - y_j)^2}{2\lambda(x_i^l + x_j^l)} \right] (x_i^l + x_j^l)^{-1}}{\exp\left(-\frac{2x_{\rm T}^l}{\lambda} \right) (2x_{\rm T}^l)^{-1} + \exp\left(-2\frac{x_{\rm B}^l}{\lambda} \right) (2x_{\rm B}^l)^{-1}}. \tag{A15}$$

This result is obtained in the limit of small polarization as the constant $\mathcal{C}$ in Eq. (A12) factorizes both in the numerator as well as in the denominator of the A matrix. At very high spin polarizations the same simplification is obtained by neglecting the minority spin contribution to the integral $I_{ij}^{\rm fm}$. The orbital polarization strength and orientation angle follow as

$$P_{\rm o}^l = \sqrt{X^2 + Z^2}, \tag{A16}$$

$$\theta_l = \arctan\left(\frac{Z}{X} \right), \tag{A17}$$

where

$$X = \frac{\left[1 - \left(\frac{\Delta x}{2\bar{x}^l} \right)^2 \right] \exp\left(-\frac{\Delta y^2}{4\lambda \bar{x}^l} \right)}{2\cosh\left(\frac{\Delta x}{\lambda} \right) + \frac{\Delta x}{\bar{x}^l} \sinh\left(\frac{\Delta x}{\lambda} \right)} \tag{A18}$$

and

$$Z = -\frac{\sinh\left(\frac{\Delta x}{\lambda} \right) + \frac{\Delta x}{2\bar{x}^l} \cosh\left(\frac{\Delta x}{\lambda} \right)}{2\cosh\left(\frac{\Delta x}{\lambda} \right) + \frac{\Delta x}{\bar{x}^l} \sinh\left(\frac{\Delta x}{\lambda} \right)} \tag{A19}$$

are the components of A^l multiplying, respectively, the σ^x and σ^z Pauli matrices, while

$$\bar{x}^l = \frac{x_{\rm T}^l + x_{\rm B}^l}{2}, \quad \Delta x = x_{\rm T}^l - x_{\rm B}^l, \quad \text{and } \Delta y = y_{\rm T} - y_{\rm B}. \tag{A20}$$

In Fig. 6, we represent the pseudospin tunneling matrix parameters $\theta_{\rm L}$ and $P_{\rm o}^{\rm L}$, as obtained from the numerical evaluation of I_{ij} combined with the definition of the pseudospin matrix in Eqs. (16), (18), and (19), plotted as a function of the relative position between the two dots measured in unit of the penetration length λ. In accordance with the general trend already observed in the SGPA, the polarization angle tends to $\pm\pi/2$ for a negative (positive) large Δx [cf. panel (a) in Fig. 6]. The switch between the extreme orientation directions becomes though smoother in the vicinity of $\Delta y = 0$, once the contributions of finite $k_\parallel$ are taken into account.

At the same time, we also notice that the strength of the pseudospin polarization does assume values in the full range between 0 and 1. In particular, well separated dots ($\Delta y \approx 4\lambda$), kept though at similar distances from the leads, yield an almost vanishing polarization strength (i.e., an incoherent tunneling). Moving toward any other geometrical configuration, the polarization strength rapidly increasing toward the maximum value of $P_{\rm o}^l = 1$.

In Fig. 6, we also indicate the contour lines corresponding to the polarization strength and orientation angle assumed in the main text. The full lines refer to the numerical calculation of the parameters. The dashed lines correspond, instead, to the analytical functions given in Eqs. (A16)–(A19). The crossing points between such pairs of lines (symmetrically distributed with respect to the axis $\Delta y = 0$) indicate microscopic realizations of the DQD junction with the desired parametrization for the tunneling rate matrices.

2. Second- and fourth-order kernels

In this section, we discuss in greater detail how to evaluate the second- and fourth-order perturbative contributions to the propagation kernel, respectively $\tilde{\mathcal{K}}^{(2)}$ and $\tilde{\mathcal{K}}^{(4)}$ as formally introduced in Eqs. (29) and (30) of the main text.

a. Coherent sequential tunneling

At first, we focus on the kernel describing the CST dynamics of interacting system with a degenerate spectrum. According to Eq. (29), such kernel reads

$$\tilde{\mathcal{K}}^{(2)} = \mathcal{P}\mathcal{L}_{\rm tun} \frac{1}{0^+ - \mathcal{L}_{\rm DQD} - \mathcal{L}_{\rm leads}} \mathcal{L}_{\rm tun}\mathcal{P}, \tag{A21}$$

with the two tunneling Liouvillians $\mathcal{L}_{\rm tun}$ defining the perturbative order. The expression 0^+ refers to the limit $\tilde{\mathcal{G}}_0 = \lim_{\lambda\to 0^+} \tilde{\mathcal{G}}_0(\lambda) = \lim_{\lambda\to 0^+} (\lambda - \mathcal{L}_{\rm DQD} - \mathcal{L}_{\rm leads})^{-1}$ which should be performed at the very end of the calculation rather than in the free propagator alone.

Within the notation for a superoperator $\mathcal{X}$, it is useful to introduce a Liouville index defined as

$$\mathcal{X}^+ \hat{\rho} := \hat{X}\hat{\rho}, \quad \mathcal{X}^- \hat{\rho} := \hat{\rho}\hat{X}, \tag{A22}$$

which allows us to reformulate a commutator as $[\hat{X}, \hat{\rho}] = \sum_\alpha \alpha \mathcal{X}^\alpha \hat{\rho}$. Using this notation for $\mathcal{L}_{\rm tun}$ yields

$$\mathcal{L}_{\rm tun}\hat{X} = -\frac{i}{\hbar} \sum_{p=\pm} \sum_{\alpha=\pm} \sum_{bn} p\, t_{b,n}^{\bar{p}}\, \mathcal{C}_b^{p,\alpha}\, \mathcal{D}_n^{\bar{p},\alpha} \hat{X} \tag{A23}$$

with n running over the four different single-particle DQD states. Beyond the α index for the different Liouville space superoperators, we further introduced in Eq. (A23) the indices $p = \pm$ and $\bar{p} = -p$ which distinguish creators ($p = +$)

from annihilator ($p = -$) and, for the tunneling amplitudes, $t^{+}_{b,n} \coloneqq t^{*}_{b,n}$ from $t^{-}_{b,n} \coloneqq t_{b,n}$. Applying this on the second-order kernel of Eq. (A21) and using the Wick contraction for lead operators, we obtain the expression

$$\tilde{\mathcal{K}}^{(2)} = \frac{-i}{2\pi} \sum_{\substack{nmp \\ l\alpha\alpha'}} \int d\varepsilon \, \Gamma^{l,p}_{n,m} \mathcal{D}^{\bar{p},\alpha_2}_{n} \frac{\alpha_1\alpha_2 f^{(p\alpha_1)}_{l}(\varepsilon)}{i0^{+} + p\varepsilon - i\hbar\mathcal{L}_{\mathrm{DQD}}} \mathcal{D}^{p,\alpha_1}_{m} \mathcal{P} \tag{A24}$$

in which, first, we add an index p also to the tunneling rate matrix $\Gamma^{l,p}_{n,m}$ and $\Gamma^{l}_{n,m} = \Gamma^{l,-}_{n,m} = \Gamma^{l,+}_{m,n}$.

The energy integration can be solved with the help of the Y^{n}_{m} function with its dimensionless variables μ and x, the dimensionless Fermi function $f^{(n)}(x)$, and the Lorentzian cutoff function $L(\tilde{W}, x) = \tilde{W}^2/(x^2 + \tilde{W}^2)$:

$$Y^{n}_{m}(\mu) \coloneqq -\frac{i}{2\pi} \int dx \frac{f^{(n)}(x) L(\tilde{W}, x)}{m(x-\mu) + i0^{+}}. \tag{A25}$$

The Lorentzian cutoff function stems from the applied wideband limit with the dimensionless wideband constant $\tilde{W} = W/(k_{\mathrm{B}}T)$ to ensure the convergence of the integration which is needed especially for the cotunneling integrals. Applying the residuum theorem, one gets for $Y^{n}_{+}(\mu)$ [38]

$$\begin{aligned} Y^{n}_{+}(\mu) &= -\frac{1}{2} f^{n}(\mu) - \frac{in}{2\pi}\left[\mathrm{Re}\Psi^{(0)}\left(\frac{1}{2} + \frac{i\mu}{2\pi}\right) - C\right] \\ &= -\frac{1}{4} - \frac{in}{2\pi}\left[\Psi^{(0)}\left(\frac{1}{2} + \frac{i\mu}{2\pi}\right) - C\right] \end{aligned} \tag{A26}$$

with the constant $C = \Psi^{(0)}[1/2 + \tilde{W}/(2\pi)]$. We furthermore introduced the digamma function

$$\Psi^{(0)}(z) \coloneqq -\sum_{n=0}^{\infty} \frac{1}{n+z} + \sum_{n=1}^{\infty} \ln\left(1 + \frac{1}{n}\right), \quad z \in \mathbb{C}. \tag{A27}$$

The constant C always disappears when summing over the α indices. Therefore, we can drop C from the CST kernel calculation. The CST Liouvillian $\mathcal{L}_{\mathrm{T}}$ and the commutator with the Lamb shift Hamiltonian introduced in Eq. (33) are the contributions of $\mathcal{K}^{(2)}$ stemming from the real and the imaginary part of the function Y^{n}_{+}, respectively.

b. Cotunneling

By including the next to leading order in the expansion of the kernel, we get a kernel which is valid up to fourth order: $\tilde{\mathcal{K}} = \tilde{\mathcal{K}}^{(2)} + \tilde{\mathcal{K}}^{(4)} + \mathcal{O}(H^{6}_{\mathrm{tun}})$. This regime of tunneling events up to fourth order in $\mathcal{L}_{\mathrm{tun}}$ is better known as the cotunneling transport regime. In this regime, two new processes are included, namely the cotunneling ones and pair tunneling ones. The fourth-order kernel can be formally split into the contributions $\tilde{\mathcal{K}}^{(4,D)}$, respectively $\tilde{\mathcal{K}}^{(4,X)}$:

$$\tilde{\mathcal{K}}^{(4,D)} = \frac{i\hbar}{(4\pi)^2} \sum_{\substack{\{l\}\{m\} \\ \{n\}\{p\} \\ \{\alpha_i\}}} \int d\varepsilon \int d\varepsilon' \mathcal{D}^{\bar{p},\alpha_4}_{n} \frac{f^{(p'\alpha_2)}_{l'}(\varepsilon')}{i0^{+} + p\varepsilon - i\hbar\mathcal{L}_{\mathrm{DQD}}} \mathcal{D}^{\bar{p}',\alpha_3}_{n'} \frac{-\alpha_1\alpha_4 \Gamma^{l,p}_{n,m}\Gamma^{l',p'}_{n',m'}}{i0^{+} + p\varepsilon + p'\varepsilon' - i\hbar\mathcal{L}_{\mathrm{DQD}}} \mathcal{D}^{p',\alpha_2}_{m'} \frac{f^{(p\alpha_1)}_{l}(\varepsilon)}{i0^{+} + p\varepsilon - i\hbar\mathcal{L}_{\mathrm{DQD}}} \mathcal{D}^{p,\alpha_1}_{m} \mathcal{P}, \tag{A28}$$

$$\tilde{\mathcal{K}}^{(4,X)} = \frac{i\hbar}{(4\pi)^2} \sum_{\substack{\{l\}\{m\} \\ \{n\}\{p\} \\ \{\alpha_i\}}} \int d\varepsilon \int d\varepsilon' \mathcal{D}^{\bar{p},\alpha_4}_{n} \frac{f^{(p'\alpha_2)}_{l'}(\varepsilon')}{i0^{+} + p\varepsilon - i\hbar\mathcal{L}_{\mathrm{DQD}}} \mathcal{D}^{\bar{p}',\alpha_3}_{n'} \frac{\alpha_1\alpha_4 \Gamma^{l,p}_{n,m}\Gamma^{l',p'}_{n',m'}}{i0^{+} + p\varepsilon + p'\varepsilon' - i\hbar\mathcal{L}_{\mathrm{DQD}}} \mathcal{D}^{p',\alpha_2}_{m'} \frac{f^{(p\alpha_1)}_{l}(\varepsilon)}{i0^{+} + p'\varepsilon' - i\hbar\mathcal{L}_{\mathrm{DQD}}} \mathcal{D}^{p,\alpha_1}_{m} \mathcal{P}. \tag{A29}$$

Equations (A28) and (A29) involve double energy integrals which can be solved by applying of the residual theorem. The generic element of the cotunneling kernel in the energy eigenbasis of the system can thus be expressed in terms of two types of functions, respectively the D and X functions, defined as

$$\begin{aligned} D^{nn'}_{pp'}(\mu, \mu', \Delta) &= -\frac{i\hbar}{4\pi^2} \int_{-\infty}^{\infty} dx \int_{-\infty}^{\infty} dx' \frac{f^{(n')}(x)}{i0^{+} + p(x-\mu)} \frac{1}{i0^{+} + px + p'x' - \Delta} \frac{f^{(n)}(x')}{i0^{+} + p(x-\mu')} \\ &= \frac{2\pi^2 n(i\pi + 2Cn')}{i\hbar(\mu - \mu')}\left[\Psi^{(0)}\left(\frac{1}{2} + \frac{i\mu}{2\pi}\right) - \Psi^{(0)}\left(\frac{1}{2} + \frac{i\mu'}{2\pi}\right)\right] - \frac{2\pi nn'}{\hbar} \sum_{k=0}^{\infty} \frac{\Psi^{(0)}\left(1 + k + \frac{i\Delta}{2\pi}\right)}{\left(k + \frac{1}{2} + \frac{i\mu}{2\pi}\right)\left(k + \frac{1}{2} + \frac{i\mu'}{2\pi}\right)} \end{aligned} \tag{A30}$$

and

$$X^{nn'}_{pp'}(\mu,\mu',\Delta) = -\frac{i\hbar}{4\pi^2}\int_{-\infty}^{\infty}dx\int_{-\infty}^{\infty}dx'\,\frac{f^{(n')}(x)}{i0^+ + p(x-\mu)}\,\frac{1}{i0^+ + px + p'x' - \Delta}\,\frac{f^{(n)}(x')}{i0^+ + p'(x'-\mu')}$$
$$= -\frac{4\pi^2}{i\hbar}\frac{nn'}{\mu+\mu'-\Delta}\Psi^{(0)}\left(\frac{1}{2}+\frac{i\mu}{2\pi}\right)\left[\Psi^{(0)}\left(\frac{1}{2}+\frac{i\mu'}{2\pi}\right)-\Psi^{(0)}\left(\frac{1}{2}+\frac{i(\Delta-\mu)}{2\pi}\right)\right]$$
$$+\frac{2\pi nn'}{\hbar}\sum_{k=0}^{\infty}\frac{\Psi^{(0)}\left(1+k+\frac{i\Delta}{2\pi}\right)}{\left(k+\frac{1}{2}+\frac{i\mu'}{2\pi}\right)\left(k+\frac{1}{2}+\frac{i(\Delta-\mu)}{2\pi}\right)}. \tag{A31}$$

There are several special cases (e.g., $\Delta = 0$) where the D and X functions can be written in closed form. Nevertheless, we refrain from elaborating all these different cases. They do not provide more physical insight, even if they can yield a speedup of the numerical calculations. The expressions for the energy integrals Eqs. (A30) and (A31) of the fourth-order kernel include both the real and the imaginary part. The latter are crucial for the calculation of the time evolution of coherences in fourth-order perturbation theory.

3. Lamb shift Hamiltonian

In this section, we derive the Lamb shift Hamiltonian for the one-particle subspace which enables us to readout the spin-resolved pseudo-exchange-field $\boldsymbol{B}_\sigma$ given in Eq. (39).

We start from the definition of the Lamb shift Hamiltonian for the one-particle subspace:

$$\hat{H}_{\mathrm{LS},1} = \sum_{li\sigma j\sigma'}\hbar\Gamma^l_{i\sigma,j\sigma'}\hat{P}_1[\hat{d}^\dagger_{i\sigma}p_l(E_1 - H_{\mathrm{DQD}})\hat{d}_{j\sigma'}$$
$$+\hat{d}_{j\sigma'}p_l(\hat{H}_{\mathrm{DQD}} - E_1)\hat{d}^\dagger_{i\sigma}]\hat{P}_1. \tag{A32}$$

Its commutator with the reduced density matrix expresses the contributions of $\tilde{K}^{(2)}$ proportional to the imaginary part of the Y^n_+ function, as defined in the previous section. Moreover, the projector on the one-particle space in Eq. (A32) reads $\hat{P}_1 = \sum_{i\sigma}\hat{d}^\dagger_{i\sigma}|\emptyset\rangle\langle\emptyset|\hat{d}_{i\sigma}$, being $|\emptyset\rangle$ the vacuum state vector.

We further proceed by inserting into Eq. (A32) the DQD Hamiltonian written in the pseudospin formulation, as given in Eq. (5), and perform a complete Taylor expansion with respect to the anisotropy component proportional to the operator $\hat{T}_z^2$. The two-particle subspace consists of a singlet and a triplet pseudospin sector; thus the relation $\hat{P}_2\hat{T}_z^2\hat{P}_2 = (\hat{P}_2\hat{T}_z^2\hat{P}_2)^n$ for $n \geqslant 1$ holds, where $\hat{P}_2$ is the projector operator on the two-particle subspace. We can thus simplify the Taylor expansion:

$$\hat{P}_2 p_l\left[\varepsilon + V + (U-V)\hat{T}_z^2\right]\hat{P}_2$$
$$= \hat{P}_2 p_l(\varepsilon+V) + \hat{P}_2\hat{T}_z^2\hat{P}_2\sum_{n=1}^{\infty}\frac{(U-V)^n}{n!}p_l^{(n)}(\varepsilon+V)$$
$$= \hat{P}_2\left\{p_l(\varepsilon+V) + \hat{T}_z^2[p_l(\varepsilon+U) - p_l(\varepsilon+V)]\right\}\hat{P}_2$$
$$= \hat{P}_2\left\{p_l(E_{2\mathrm{g}1}) + \hat{T}_z^2[p_l(E_{2\mathrm{e}1}) - p_l(E_{2\mathrm{g}1})]\right\}\hat{P}_2. \tag{A33}$$

At this stage, the operator identity is useful:

$$\hat{P}_1\hat{d}_{j\sigma'}\hat{T}_z^2\hat{d}^\dagger_{i\sigma}\hat{P}_1 = \frac{1}{2}\hat{P}_1\hat{d}_{j\sigma'}\hat{d}^\dagger_{i\sigma}\hat{P}_1 + \sum_k\sigma^z_{ki}\hat{P}_1\hat{d}_{j\sigma'}\hat{d}^\dagger_{k\sigma}\hat{T}_z\hat{P}_1. \tag{A34}$$

Some algebra leads, eventually, to the formulation of the Lamb shift Hamiltonian, obtained under the additional assumption of parallel spin polarization of the leads:

$$\hat{H}_{\mathrm{LS},1} = \sum_l\hbar\Gamma^l_0[p_l(E_{10}) + 2p_l(E_{2\mathrm{g}1}) + p_l(E_{2\mathrm{e}1})]\hat{P}_1$$
$$+\sum_l\hbar\Gamma^l_0(D_\uparrow - D_\downarrow)[p_l(E_{10}) - p_l(E_{2\mathrm{e}1})]\boldsymbol{n}^l_{\mathrm{s}}\cdot\hat{P}_1\hat{\boldsymbol{S}}\hat{P}_1$$
$$+\sum_{l\sigma}2\hbar\Gamma^l_0D_\sigma[p_l(E_{10}) - p_l(E_{2\mathrm{g}1})]P_{\mathrm{o}}\boldsymbol{n}^l_{\mathrm{o}}\cdot\hat{P}_\sigma\hat{\boldsymbol{T}}\hat{P}_\sigma$$
$$+\sum_{l\sigma}2\hbar\Gamma^l_0D_{\bar{\sigma}}[p_l(E_{2\mathrm{e}1}) - p_l(E_{2\mathrm{g}1})]P_{\mathrm{o}}(\boldsymbol{n}^l_{\mathrm{o}}\cdot\boldsymbol{e}_z)\hat{P}_\sigma\hat{T}_z\hat{P}_\sigma, \tag{A35}$$

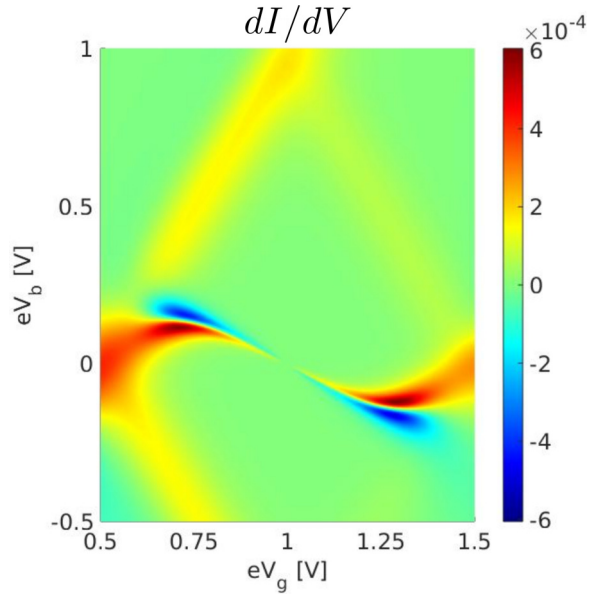

FIG. 7. Differential conductance for $P_{\mathrm{s}} = 0.99$ and constant interaction ($U = V$): The stability diagram of a DQD shows only one pseudospin resonance in comparison with Fig. 2(d) where two resonances for the different spin species appear. Changing the spin polarization at constant interaction does not alter the differential conductance in agreement with Eq. (39). The parameters are the following: $U = 1V$, $k_{\mathrm{B}}T = 0.05V$, $P_{\mathrm{o}} = 0.99$, $\theta = 0.95\pi$, $\Gamma^{\mathrm{R}}_0 = 2.5\times 10^{-3}\,V = 2\Gamma^{\mathrm{L}}_0$, $\varepsilon_0 = -2V$, and $W = 250V$ (bandwidth).

where the spin operator $\hat{\boldsymbol{S}}$, similarly to the pseudospin one defined in Eq. (3), reads, in components,

$$\hat{S}_\alpha = \frac{1}{2}\sum_{i\tau\tau'} \hat{d}^\dagger_{i\tau}\sigma^\alpha_{\tau\tau'}\hat{d}_{i\tau'}. \tag{A36}$$

The first and the second term in Eq. (A35) do not contribute to the time evolution of the reduced density matrix, which is block diagonal in spin as the parallel spin polarization of the leads defines a common quantization axis for the entire DQD junction. Thus, the Lamb shift Hamiltonian reduces, effectively, to a pseudospin Zeeman term:

$$\tilde{\hat{H}}_{\mathrm{LS},1} = \sum_\sigma \hbar \boldsymbol{B}_\sigma \cdot \hat{\boldsymbol{T}}_\sigma, \tag{A37}$$

where we have introduced the spin-resolved pseudo-exchange-field

$$\begin{aligned}\boldsymbol{B}_\sigma = \sum_l 2P_{\mathrm{o}}\Gamma^l_0 \big\{ & D_\sigma[p_l(E_{10}) - p_l(E_{2\mathrm{g}1})]\boldsymbol{n}^l_{\mathrm{o}} \\ & + D_{\bar{\sigma}}[p_l(E_{2\mathrm{e}1}) - p_l(E_{2\mathrm{g}1})]\big(\boldsymbol{n}^l_{\mathrm{o}}\cdot\boldsymbol{e}_z\big)\boldsymbol{e}_z\big\}\end{aligned} \tag{A38}$$

and the pseudospin operator

$$\hat{\boldsymbol{T}}_\sigma = \hat{P}_\sigma \hat{\boldsymbol{T}} \hat{P}_\sigma. \tag{A39}$$

It is now straightforward to demonstrate that, in the equation of motion for the expectation value of the pseudospin, the commutator with the Lamb shift Hamiltonian contributes with the precession dynamics captured by the last term in Eq. (38):

$$-\frac{i}{\hbar}[\hat{H}_{\mathrm{LS},1}\hat{\rho}_{\mathrm{red},1}] \Longleftrightarrow \boldsymbol{B}_\sigma \times \boldsymbol{T}_\sigma. \tag{A40}$$

By assuming a constant interaction ($U = V$), the energy differences $E_{2\mathrm{e}1}$ and $E_{2\mathrm{g}1}$ coincide. This implies that also the last term of Eq. (A35) vanishes and the spin-resolved exchange fields are collinear. Consequently, only one pseudospin resonance is present in the stability diagram (cf. Fig. 7), independently of the spin polarization of the leads. The figure clearly indicates that the pseudospin anisotropy is a necessary condition of the emergence of the synthetic SOI.

[1] Effectively degenerate are all states with an energy separation smaller than the tunneling-induced broadening.
[2] J. König and J. Martinek, Phys. Rev. Lett. **90**, 166602 (2003).
[3] M. Braun, J. König, and J. Martinek, Phys. Rev. B **70**, 195345 (2004).
[4] S. Braig and P. W. Brouwer, Phys. Rev. B **71**, 195324 (2005).
[5] W. Rudziński, J. Barnaś, R. Świrkowicz, and M. Wilczyński, Phys. Rev. B **71**, 205307 (2005).
[6] I. Weymann, J. König, J. Martinek, J. Barnaś, and G. Schön, Phys. Rev. B **72**, 115334 (2005).
[7] R. Hornberger, S. Koller, G. Begemann, A. Donarini, and M. Grifoni, Phys. Rev. B **77**, 245313 (2008).
[8] L. Y. Zhang, C. Y. Wang, Y. G. Wei, X. Y. Liu, and D. Davidović, Phys. Rev. B **72**, 155445 (2005).
[9] K. Hamaya, M. Kitabatake, K. Shibata, M. Jung, M. Kawamura, K. Hirakawa, T. Machida, T. Taniyama, S. Ishida, and Y. Arakawa, Appl. Phys. Lett. **91**, 022107 (2007).
[10] N. M. Gergs, S. A. Bender, R. A. Duine, and D. Schuricht, Phys. Rev. Lett. **120**, 017701 (2018).
[11] M. Hell, B. Sothmann, M. Leijnse, M. R. Wegewijs, and J. König, Phys. Rev. B **91**, 195404 (2015).
[12] D. Darau, G. Begemann, A. Donarini, and M. Grifoni, Phys. Rev. B **79**, 235404 (2009).
[13] M. G. Schultz, Phys. Rev. B **82**, 155408 (2010).
[14] H. A. Nilsson, O. Karlström, M. Larsson, P. Caroff, J. N. Pedersen, L. Samuelson, A. Wacker, L.-E. Wernersson, and H. Q. Xu, Phys. Rev. Lett. **104**, 186804 (2010).
[15] O. Karlström, J. N. Pedersen, P. Samuelsson, and A. Wacker, Phys. Rev. B **83**, 205412 (2011).
[16] J. König and Y. Gefen, Phys. Rev. B **65**, 045316 (2002).
[17] B. Michaelis, C. Emary, and C. W. J. Beenakker, Europhys. Lett. **73**, 677 (2006).
[18] S. Gustavsson, R. Leturcq, M. Studer, T. Ihn, K. Ensslin, D. C. Driscoll, and A. C. Gossard, Nano Lett. **8**, 2547 (2008).
[19] P. Trocha, I. Weymann, and J. Barnaś, Phys. Rev. B **80**, 165333 (2009).
[20] A. Donarini, G. Begemann, and M. Grifoni, Phys. Rev. B **82**, 125451 (2010).
[21] T. Hatano, T. Kubo, Y. Tokura, S. Amaha, S. Teraoka, and S. Tarucha, Phys. Rev. Lett. **106**, 076801 (2011).
[22] M. Niklas, A. Trottmann, A. Donarini, and M. Grifoni, Phys. Rev. B **95**, 115133 (2017).
[23] M. H. Hettler, W. Wenzel, M. R. Wegewijs, and H. Schoeller, Phys. Rev. Lett. **90**, 076805 (2003).
[24] G. Begemann, D. Darau, A. Donarini, and M. Grifoni, Phys. Rev. B **77**, 201406(R) (2008).
[25] A. Donarini, M. Niklas, M. Schafberger, N. Paradiso, C. Strunk, and M. Grifoni, Nat. Commun. **10**, 381 (2019).
[26] I. Weymann, R. Chirla, P. Trocha, and C. P. Moca, Phys. Rev. B **97**, 085404 (2018).
[27] M. T. Maurer, J. König, and H. Schoeller, Phys. Rev. Res. **2**, 033440 (2020).
[28] A. Donarini, *Many-Body Methods for Real Materials*, edited by E. Pavarini, E. Koch, and S. Zhang (Verlag des Forschungszentrum Jülich, Jülich, 2019), pp. 393–419.
[29] In another context, these matrices are called tunneling self-energies.
[30] M. Margańska, D. R. Schmid, A. Dirnaichner, P. L. Stiller, C. Strunk, M. Grifoni, and A. K. Hüttel, Phys. Rev. Lett. **122**, 086802 (2019).
[31] S. Nakajima, Prog. Theor. Phys. **20**, 948 (1958).
[32] R. Zwanzig, J. Chem. Phys. **33**, 1338 (1960).
[33] H. P. Breuer and F. Petruccione, *The Theory of Open Quantum Systems* (Oxford University Press, New York, 2002).
[34] S. Koller, M. Grifoni, M. Leijnse, and M. R. Wegewijs, Phys. Rev. B **82**, 235307 (2010).
[35] M. Leijnse, Ph.D. thesis, RWTH Aachen University, 2010.
[36] S. Koller, Ph.D. thesis, University of Regensburg, 2010.
[37] M. Niklas, Ph.D. thesis, University of Regensburg, 2018.

[38] D. Mantelli, Ph.D. thesis, University of Regensburg, 2016.
[39] M. Milgram, arXiv:math/0406338.
[40] J. Barański, T. Zienkiewicz, M. Barańska, and K. J. Kapcia, Sci. Rep. **10**, 2881 (2020).
[41] M. E. Torio, K. Hallberg, S. Flach, A. E. Miroshnichenko, and M. Titov, Eur. Phys. J. B **37**, 399 (2004).
[42] A. Bärnthaler, S. Rotter, F. Libisch, J. Burgdörfer, S. Gehler, U. Kuhl, and H.-J. Stöckmann, Phys. Rev. Lett. **105**, 056801 (2010).
[43] Y. Joe, J. Kim, E. Hedin, R. Cosby, and A. Satanin, J. Comput. Electron. **4**, 129 (2005).
[44] A. C. Johnson, C. M. Marcus, M. P. Hanson, and A. C. Gossard, Phys. Rev. Lett. **93**, 106803 (2004).
[45] In a more realistic setup, the vacuum level would be replaced by the top of the valence band of the insulator separating the metallic lead from the dot. The essence of the model remains, though, unchanged.
[46] J. Tersoff and D. R. Hamann, Phys. Rev. B **31**, 805 (1985).